

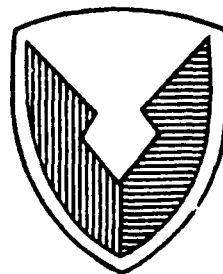
AD-A220 136



AD No. _____

TECOM Project No. 7-CO-R87-DP0-017

DPG No. DPG-FR-89-711



US ARMY
MATERIEL COMMAND

FINAL REPORT

DUGWAY OPTICAL CLIMATOLOGY STUDY

BY

CHRISTOPHER A. BILTOFT
RICK D. EWALD

Meteorology Division
Materiel Test Directorate

U. S. ARMY DUGWAY PROVING GROUND
DUGWAY, UTAH 84022-5000

December 1988

APPROVED FOR PUBLIC RELEASE; DISTRIBUTION UNLIMITED

90 04 05 011

Disposition Instructions

Destroy this report when no longer needed. Do not return it to the originator.

Disclaimer Statement

The views, opinions, and findings in this report are those of the authors and should not be construed as an official Department of the Army position, unless so designated by other official documentation.

Trade Name Statement

The use of trade names in this report does not constitute an official endorsement or approval of the use of such commercial hardware or software. This report may not be cited for purposes of advertisement.



REPLY TO
ATTENTION OF

DEPARTMENT OF THE ARMY
HEADQUARTERS, U.S. ARMY TEST AND EVALUATION COMMAND
ABERDEEN PROVING GROUND, MARYLAND 21005-5055



22 FEB 1990

AMSTE-TC-M (70-10p)

MEMORANDUM FOR Commander, U.S. Army Dugway Proving Ground,
ATTN: STEDP-MT-M, Dugway, UT 84022-5000

SUBJECT: Final Report: Dugway Optical Climatology Study

1. Subject report is approved.
2. Point of contact at this headquarters is Mr. James Piro,
AMSTE-TC-M, amstetcm@apg-emh4.apg.army.mil, AUTOVON
298-3677/2170.

FOR THE COMMANDER:

GROVER H. SHELTON
Chief, Meth Imprv Div
Directorate for Technology

Accession No.	
NTIS GEN. NO.	
DTIC INFO.	
Unpublished	
Justification	
FJ	
Distribution	
Availability Code	
Dist	Avail. Period
	Spec. Civil

A-1



REPORT DOCUMENTATION PAGE

1a. REPORT SECURITY CLASSIFICATION UNCLASSIFIED		1b. RESTRICTIVE MARKINGS										
2a. SECURITY CLASSIFICATION AUTHORITY		3. DISTRIBUTION/AVAILABILITY OF REPORT Approved for Public Release; Distribution unlimited										
2b. DECLASSIFICATION/DOWNGRADING SCHEDULE												
4. PERFORMING ORGANIZATION REPORT NUMBER(S) DPG-FR-89-711		5. MONITORING ORGANIZATION REPORT NUMBER(S)										
6a. NAME OF PERFORMING ORGANIZATION U.S. Army Dugway Proving Ground	6b. OFFICE SYMBOL <i>(If applicable)</i> STEDP-MT-M	7a. NAME OF MONITORING ORGANIZATION										
6c. ADDRESS (City, State, and ZIP Code) Dugway, UT 84022-5000		7b. ADDRESS (City, State, and ZIP Code)										
8a. NAME OF FUNDING/SPONSORING ORGANIZATION PM Smoke/Obscurants	8b. OFFICE SYMBOL <i>(If applicable)</i> AMCPEO-CNS-AM	9. PROCUREMENT INSTRUMENT IDENTIFICATION NUMBER										
8c. ADDRESS (City, State, and ZIP Code) Aberdeen Proving Ground, MD 21005-5001		10. SOURCE OF FUNDING NUMBERS PROGRAM ELEMENT NO.	PROJECT NO. R87-DPO-017									
11. TITLE (Include Security Classification) Dugway Optical Climatology Study (UNCLASSIFIED)		TASK NO.	WORK UNIT ACCESSION NO.									
12. PERSONAL AUTHOR(S) Biltoft, Christopher A. and Ewald, Rick D.	13a. TYPE OF REPORT Methodology Report											
13b. TIME COVERED FROM Feb 88 TO Dec 88	14. DATE OF REPORT (Year Month Day) 21 December 1988											
15. PAGE COUNT												
16. SUPPLEMENTARY NOTATION												
17. COSATI CODES <table border="1"><tr><th>FIELD</th><th>GROUP</th><th>SUB-GROUP</th></tr><tr><td>04</td><td>02</td><td></td></tr><tr><td></td><td></td><td></td></tr></table>	FIELD	GROUP	SUB-GROUP	04	02					18. SUBJECT TERMS (Continue on reverse if necessary and identify by block number) scintillation, humidity flux, millimeter-wave, refractive index structure parameter, temperature flux, temperature-humidity coherence, <i>Atmospheric turbulence effects on optical (visible-wavelength) and millimeter-wavelength (mmw) wave propagation can be described by the refractive index structure parameter C_N^2. Field measurements were made in February and August 1988 at U.S. Army Dugway Proving Ground (DPG) to verify mathematical relationships between the optical (visible-wavelength) and millimeter-wavelength (mmw) refractive index structure parameters C_N^2 and three meteorological variables: (1) the temperature structure parameter C_T^2, (2) the humidity structure parameter C_q^2, and (3) the temperature-humidity structure parameter C_{Tq}. Using certain assumptions, these structure parameters can be estimated from (Cont'd on next page)</i>		
FIELD	GROUP	SUB-GROUP										
04	02											
20. DISTRIBUTION/AVAILABILITY OF ABSTRACT <input checked="" type="checkbox"/> UNCLASSIFIED/UNLIMITED <input type="checkbox"/> SAME AS RPT <input type="checkbox"/> DTIC USERS	21. ABSTRACT SECURITY CLASSIFICATION UNCLASSIFIED											
22a. NAME OF RESPONSIBLE INDIVIDUAL Christopher A. Biltoft	22b. TELEPHONE (Include Area Code) (801)831-5101		22c. OFFICE SYMBOL STEDP-MT-M									

19. ABSTRACT (CONT'D)

measurements of the atmospheric fluxes of sensible heat and latent heat (humidity). The optical C_N^2 computed for daytime conditions agreed well with the C_N^2 measured by an optical scintillometer. However, because of the intermittency of turbulence in the stable nighttime atmosphere, the heat and humidity fluxes exhibited considerable variability in space and time. Consequently, the optical C_N^2 calculated using flux measurements at a point showed considerable scatter about the path-averaged optical C_N^2 measured by the scintillometer. Both incident short-wave and net radiation were found to be convenient indicators of temporal variations in optical C_N^2 during the day, but not at night.

1473,821 19

Existing theory relates mmw C_N^2 to C_T^2 , C_q^2 , and C_{Tq} . The temperature-humidity cross-structure correlation r_{Tq} must be known to estimate C_{Tq} . In the absence of direct measurements of r_{Tq} , it is usually approximated by a constant between zero and unity. Previous studies over moist soils have indicated that r_{Tq} is near unity, while the present DPG study over dry soil indicates that it is near zero. A possible explanation for the DPG results is the lack of moisture available for evaporation from the strongly heated ground surface. The previous tests of the mmw C_N^2 theory over moist soils have confirmed that mmw C_N^2 is principally determined by the C_q^2 contribution, with a secondary contribution from C_{Tq} . However, in the case of a dry surface, C_{Tq} can become the dominant term, depending on the magnitude of r_{Tq} . Rather than make assumptions about the magnitude of r_{Tq} , it is therefore preferable to obtain fast-response (10-Hz) temperature and humidity measurements and use spectrum analysis techniques to determine r_{Tq} . With r_{Tq} known, mmw C_N^2 can be estimated using heat and moisture flux measurements.

TABLE OF CONTENTS

	<u>Page</u>
ACKNOWLEDGMENTS	ii
<u>SECTION 1. SUMMARY</u>	
1.1 BACKGROUND	1
1.2 STUDY OBJECTIVE	1
1.3 INSTRUMENTATION	1
1.4 RESULTS	2
1.5 CONCLUSIONS	4
1.6 RECOMMENDATIONS	5
<u>SECTION 2. DETAILS OF THE TEST</u>	
2.1 SITE DESCRIPTION	7
2.2 TEST DESIGN AND INSTRUMENTATION	8
2.3 RELATIONSHIP OF C_N^2 TO OTHER ATMOSPHERIC VARIABLES	13
2.4 DATA SCREENING AND ANALYSES	16
2.5 CALCULATION OF OPTICAL AND MILLIMETER-WAVE C_N^2 FROM FLUXES . .	26
2.6 COMPARISONS OF ACTINOMETER AND SCINTILLOMETER DATA	31
<u>SECTION 3. APPENDICES</u>	
A DESCRIPTION OF SCINTILLOMETER OPERATION	A-1
B DESCRIPTION OF DPG SPECTRUM ANALYSIS PROGRAM	B-1
C LIST OF SYMBOLS	C-1
D REFERENCES	D-1

ACKNOWLEDGMENTS

Dugway Proving Ground (DPG) optical climatology field data were collected in February and August 1988 by the DPG Materiel Test Directorate. Mr. Martin Kogut of the Instrumentation Branch, Test Data Division provided instrumentation and data collection support during both the February and August phases of the study. Under Task Assignment M-6 of Contract No. DAAD09-87-D-0038 with the H. E. Cramer Company, Inc., Messrs. Bertran Tanner, Joel Green, and Craig Knox of Campbell Scientific, Inc. provided additional instrumentation support during the August phase of the study. Photographic support was provided by Mr. Ogden Kraut of the Audio-Visual Branch, Test Data Division and typing support was provided by Mrs. Susan Gross of the Meteorology Division. The optical climatology study was partially supported by funds provided by the Program Manager, Smoke/Obscurants. The DPG project officer for smoke methodology development is Mr. Dennis Bodrero of the Smoke/Obscurants Branch, Test Management Division.

SECTION 1. SUMMARY

1.1 BACKGROUND

Interest in the use of wave propagation techniques for military target acquisition has been steadily increasing over the last few decades. The performance of sensors based on these techniques is determined in part by the refractive index fluctuations over the line of sight between the sensor and the target. Because the effects of these fluctuations can be described by the refractive index structure parameter C_N^2 , studies have been performed to define C_N^2 as a function of meteorological variables such as the temperature structure parameter C_T^2 , the humidity structure parameter C_q^2 , and the temperature-humidity structure parameter C_{Tq} . These parameters can in turn be related to the atmospheric fluxes of sensible heat and latent heat (humidity).

U.S. Army Dugway Proving Ground (DPG) has "optical" scintillometers that are used to measure C_N^2 for the visible wavelengths, but these measurements are not made with sufficient regularity to develop an "optical climatology" for test planning purposes. Also, no instrumentation is available to measure C_N^2 in other wavelengths, in particular the millimeter wavelengths (mmw), of special interest for planned field tests. Consequently, it is desirable to establish working relationships between C_N^2 at various wavelengths and readily measured variables.

1.2 STUDY OBJECTIVE

The objective of the optical climatology study was to define and test methodologies for deriving optical and mmw C_N^2 from available meteorological measurements at DPG.

1.3 INSTRUMENTATION

The principal instrumentation used in this study included an optical scintillometer, actinometers, and fast-response vertical velocity, temperature, and humidity sensors. The scintillometer consisted of a transmitter

with a 0.94- μm light emitting diode (LED) source and a downrange receiver. Scintillation measurements were obtained as a function of the variance of signal intensity at the receiver. Single-axis sonic anemometer/thermometers were used to measure vertical velocity variances and the covariances of temperature with vertical velocity, from which sensible heat flux is derived. A fast-response hygrometer was mounted alongside each sonic anemometer/thermometer to obtain humidity variances and covariances of humidity with temperature and vertical velocity. Actinometers included pyranometers for short-wave radiation and pyrgeometers for long-wave radiation mounted to measure incoming and outgoing radiation at 1.4 m above ground level (AGL).

A 2-m AGL optical scintillometer path was selected at a location representative of the DPG test grid terrain. The paths chosen for the summer and winter trials differed because of the requirement to keep direct sunlight out of the scintillometer optics. Four sets of the fast-response sensors and the actinometers were located near the scintillometer receiver. The fast-response instrument sets were placed in an east-west line with 6-m separation between each set. Three of these sets were mounted at 3.5 m AGL and one was mounted at 1.5 m AGL. Located near this instrument cluster were two 10-m meteorological towers instrumented for wind measurements at 10 m and temperature and humidity measurements at 2 m. Data were collected from the fast-response instruments at 10 Hz, and from the other instruments at 1 Hz. The 1-Hz data were averaged into 1-min data points for storage.

1.4 RESULTS

Data were collected during two phases: (a) Phase I in February 1988 to represent winter conditions and (b) Phase II in August 1988 to represent summer conditions. Many of the desired instruments were unavailable or malfunctioned during Phase I. Consequently, analyses of data from this phase mainly addressed relationships between incoming short-wave radiation and C_N^2 . During Phase II, flux and variance data were available from the fast-response instrumentation and were used to derive C_N^2 values for comparison with the values obtained from the scintillometer measurements. Phase II actinometer data were also compared with scintillometer C_N^2 measurements.

The Phase II data were used to estimate the contributions to C_N^2 by the fluxes of heat and humidity and the temperature-humidity covariance. Over a strongly heated dry surface (typical of midday conditions at DPG during the summer), the upward heat flux from the ground surface is the major contributor to optical C_N^2 . The upward humidity flux contributes only a tenth to a hundredth of a percent to the optical C_N^2 and can be safely disregarded, while the temperature-humidity covariance term contributes between 1 and 5 percent. At night, the heat flux is downward towards the surface while the humidity flux remains upwards. The nocturnal heat flux is 10 percent or less of the midday flux, and the nocturnal moisture flux remains small, contributing negligibly to C_N^2 .

A major difference between the findings of this study and previous studies conducted in more humid conditions is that the coherence, or frequency-dependent correlation between temperature and humidity, is much less than unity. Temperature-humidity coherence at midday tends to fall below 0.75 for eddy sizes of 10 m or less, due to the lack of moisture available for evaporation at the dry surface. At night, coherence remains low for all scales of motion. Nocturnal conditions at DPG are characterized by light winds, stable thermal stratification, and intermittent turbulence. The small amounts of moisture available at the surface often do not rise through the overlying layers. Thermally stratified layers are subjected to differential rates of cooling, depending on moisture content and contact with the cooler surface. Coherence is diminished as thermally isolated layers, drifting about in light winds, pass over sensors during sampling periods.

The optical C_N^2 computed for daytime conditions were consistent with and comparable (within ± 30 percent) to measured C_N^2 . However, the C_N^2 derived from nocturnal flux and covariance measurements exhibited considerable scatter between instrument sets and differed from the optical path-averaged C_N^2 measurements by up to several orders of magnitude. The intermittency of turbulence in strongly stable nocturnal conditions experienced at DPG adds a high degree of uncertainty to estimates of C_N^2 .

usual assumption that the temperature-humidity coherence is unity, is larger than the temperature and humidity terms. If this assumption is correct, the cross-structure term nearly cancels the temperature and humidity terms in the C_N^2 equation, producing very low mmw C_N^2 in dry desert conditions. Analysis of the DPG temperature-humidity cross-spectra suggests that the temperature-humidity coherence is closer to zero than unity. These results cannot be verified against actual mmw C_N^2 measurements because the instrumentation required to obtain these measurements is not available at DPG.

Intercomparisons between optical scintillometer C_N^2 measurements and incoming short-wave and net radiation during both Phases I and II indicated that they covary during daylight hours. No relationship between nocturnal net radiation and optical C_N^2 was found.

1.5 CONCLUSIONS

Relationships between optical C_N^2 and heat flux were verified for midday over typical (summertime) DPG test grid conditions. If a heat flux measurement is available, it is possible to calculate optical C_N^2 (or vice versa) with a high degree of reliability. Because C_N^2 can easily vary over an order of magnitude depending on the underlying ground conditions, terrain variability is the greatest source of uncertainty in the computation procedure.

Incident short-wave radiation or net radiation measurements can provide valuable information on temporal variations in C_N^2 during daylight hours. The relationship between radiation and C_N^2 is relative rather than absolute because the magnitude of C_N^2 is also dependent upon ground conditions and wind speed. Nevertheless, radiation measurements provide a simple, inexpensive means to monitor C_N^2 and to track it through changes in cloud cover.

The relationship between path-averaged C_N^2 measurements and point measurements of heat flux at night is tenuous. The nocturnal atmosphere is highly stratified, with significant variability in space and time. Nocturnal turbulence also exhibits a high degree of intermittency. For these reasons, flux measurements made at a point are not likely to be representative of conditions existing along an extended optical path. The point-to-point measurement variability at the adjacent fast-response instrument sites was of approximately the same magnitude as the variability between the sites and the optical path. A more general conclusion is that nocturnal meteorological measurements made at one location are not likely to be representative of conditions at other nearby locations.

The real component of the mmw refractive index is composed of a temperature structure, a humidity structure, and a temperature-humidity cross-structure term. The magnitude of the cross-structure term is dependent upon the temperature-humidity coherence. Previous mmw studies conducted over moist soils conclude that the humidity structure term is the dominant contributor to mmw C_N^2 , and that temperature-humidity coherence is near unity. The present study indicates that, over dry soils, the temperature-humidity cross-structure term would be dominant if it were not diminished by a temperature-humidity coherence much less than unity. Because of the variability in temperature-humidity coherence, it is necessary to use fast-response temperature and humidity measurements and spectrum analysis techniques to specify turbulence effects on mmw propagation.

1.6 RECOMMENDATIONS

The fast-response data sets collected during Phase II testing contain roughly 40 megabytes of high quality data. Only a small sample of the available data set was used to generate the results presented in this report. Interesting features not addressed in this report include the details of flux transition through sunrise and the presence of intermittent turbulence bursts at night that cause a temporary breakdown of the stability structure. Analysis of this data set should continue.

Insufficient data were collected during Phase I to analyze the relationship of wintertime fluxes to C_N^2 . The behavior of the humidity flux term over wet or snow covered surfaces is likely to be considerably different from the present dry ground results. These effects can be particularly significant for mmw propagation. A second winter measurement project should be initiated after DPG acquires its fast-response hygrometers and a digital data collection system.

Millimeter-wave C_N^2 cannot be calculated with certainty over dry soils until the effects of temperature-humidity coherence on the temperature-humidity cross-structure term are determined. Co-located fast-response temperature and humidity instruments, with alias-free data rates to 10 Hz, should be used during mmw field experiments to determine this coherence, which can be applied as a multiplication factor on the cross-structure term. With this modification, the mmw turbulence theory, verified for moist conditions during the Flatville, Illinois experiments (Hill et al., 1988), can be used over dry soils.

SECTION 2. DETAILS OF THE TEST

2.1 SITE DESCRIPTION

Most DPG test grids are located on flat clay soil covered with a desert shrub type vegetation. The location chosen for the optical climatology test as being representative of these test grids was between the Atmospheric Sciences Laboratory (ASL) rawinsonde building (Building 4000) and Avery Area (Figure 1). This site has the added convenience of readily available electric power and two 10-m meteorological masts instrumented to provide continuous information on temperature, relative humidity, wind direction, and wind speed. Pressure and radiation data are also continuously available at the Building 4000 site.

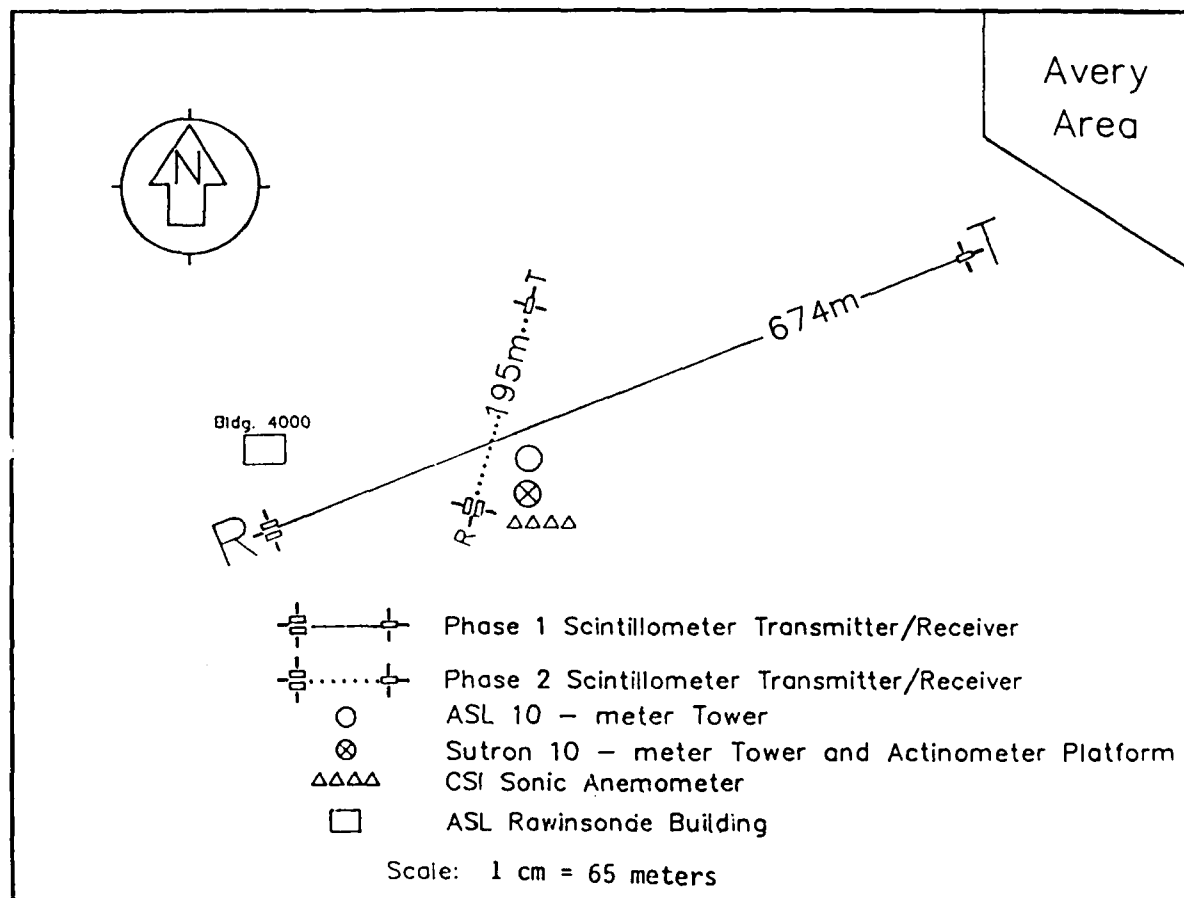


Figure 1. Optical Climatology Study Site.

The Building 4000 site is located on the north eastern corner of the Ditto Technical Center, several hundred meters south of the eastern end of the Michael Army Airfield runway. There are no significant topographical features within 1 km of the site from the northwest quadrant clockwise to the southeast quadrant. Several obstructions (trees, buildings, water tower) and a creek bed are within 1 km of the site in the southwest quadrant. Because an unobstructed fetch of 300 to 1000 m was desired for atmospheric flux measurements, Phase II trials were restricted to periods with either wind directions from northeast to southeast or light and variable winds.

The major difficulty encountered at the Building 4000 site was finding a suitable scintillometer path. The optical path had to be over relatively undisturbed land and fit within the physical constraints of the runway, buildings, and roads. An additional constraint was that scintillometer transmitter and receiver optics had to be protected from direct exposure to sunlight, which can occur when the sun is at low angles above the horizon. The scintillometer path was changed between Phases I and II in order to protect the optics during trials at sunrise and sunset.

2.2 TEST DESIGN AND INSTRUMENTATION

The DPG instrumentation used during Phase I included a scintillometer, a three-axis sonic anemometer, the instrumentation on two 10-m masts, and a set of actinometers mounted on a platform. Additional instrumentation for Phase II was provided and operated by Campbell Scientific, Inc. (CSI). These sensors included four sets of single-axis sonic anemometers, fine-wire thermocouples, and krypton hygrometers. The three-axis sonic anemometer was not used during Phase II.

An optical scintillometer (Figure 2), as described in Ochs and Cartwright (1980), was used to measure the refractive index structure parameter C_N^2 . The scintillometer consists of a transmitter using a 0.94- μm LED source and a pair of downrange receivers. The log intensity variance in irradiance at the receiver is used as a measure of C_N^2 (see Appendix A). Scintillometer measurements were taken at a height of 2 m above the surface. The Phase I

path length was 674 m, while the Phase II path length was 195 m. Power for the scintillometer transmitters was provided by storage batteries.

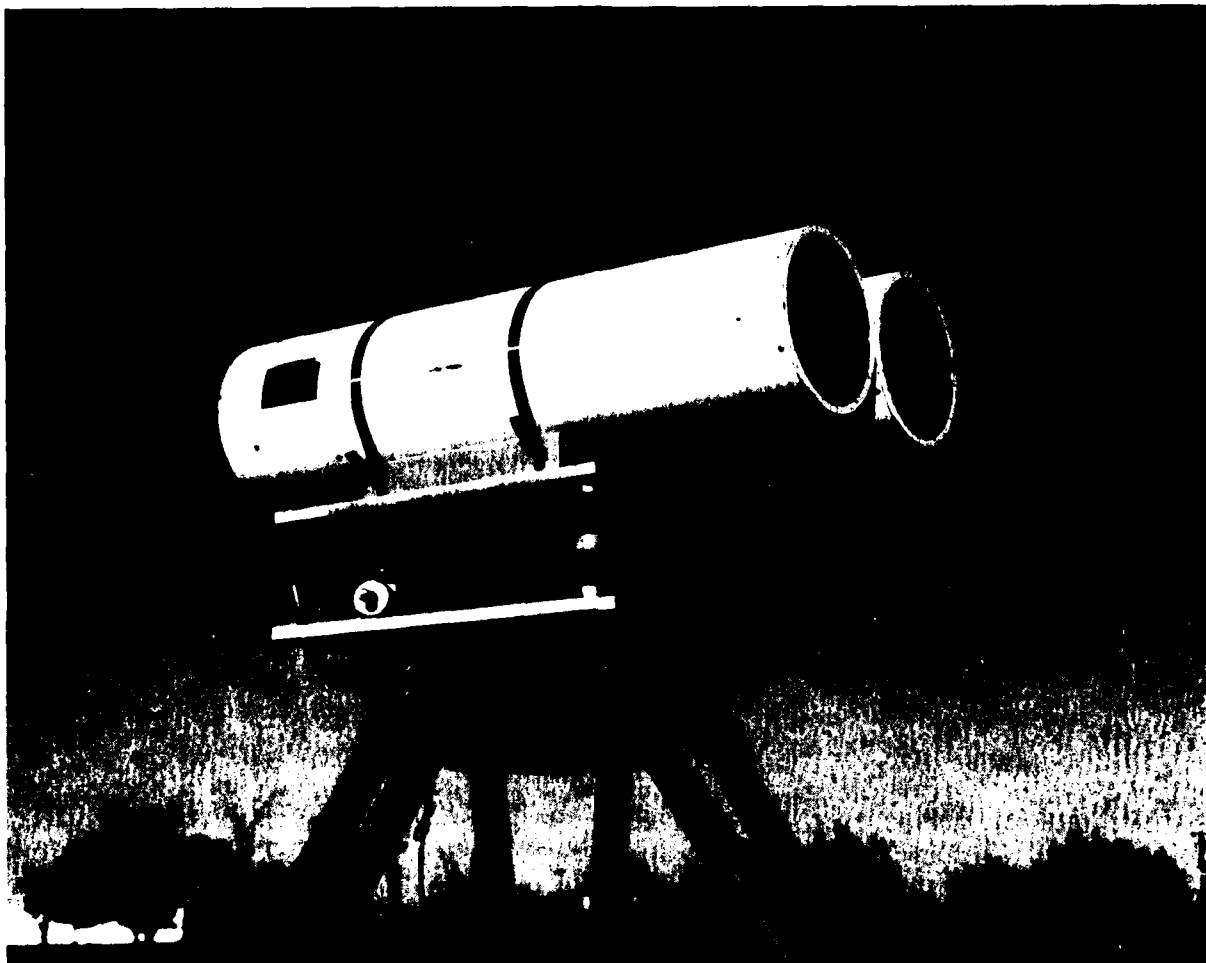


Figure 2. Model IV Optical Scintillometer Receiver.

Actinometer data were taken from two Eppley precision spectral pyranometers and two Eppley pyrgeometers, as described in the Eppley Laboratory manual. These instruments were mounted on an actinometer platform (Figure 3) to measure incident and reflected short-wave radiation and incident and emitted long-wave radiation. The combination of these measurements produced net radiation.

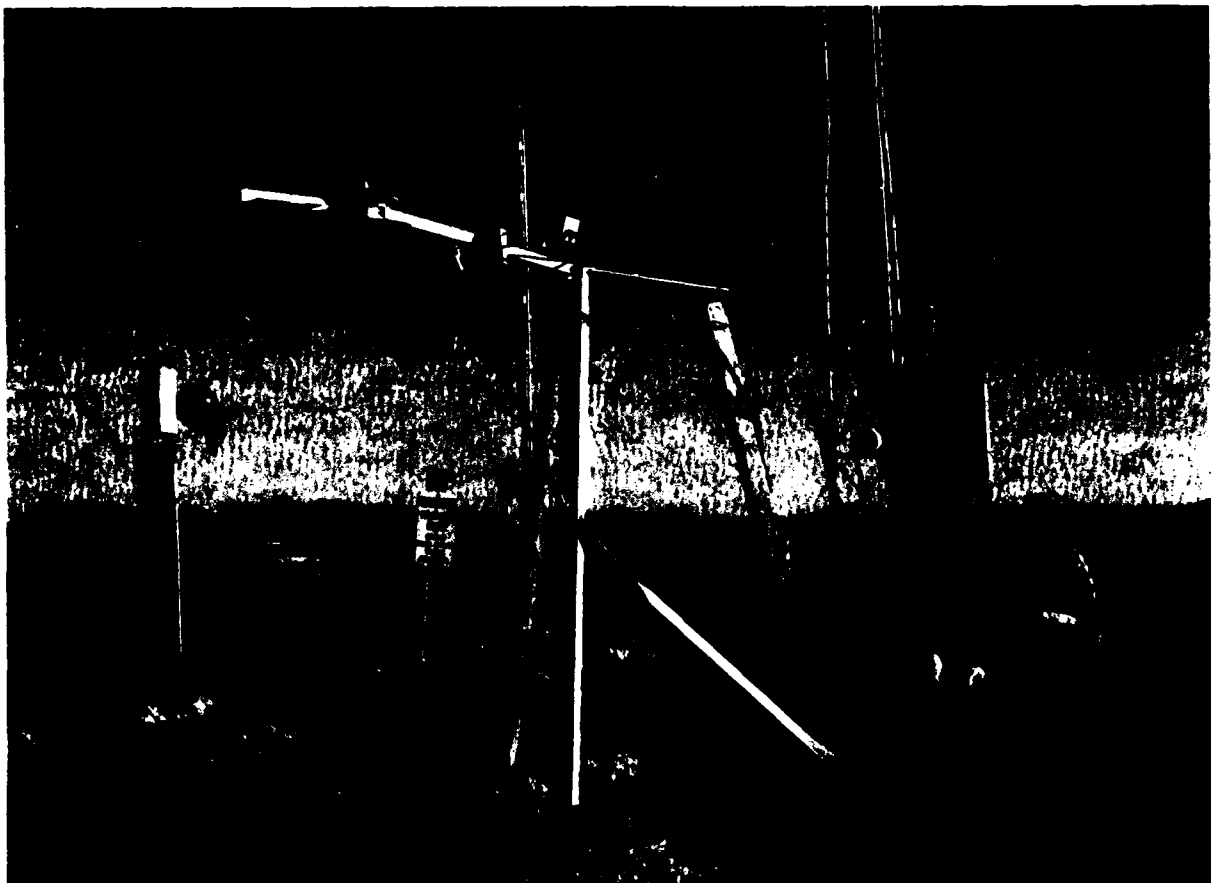


Figure 3. DPG Actinometer Platform.

Low battery voltages were found for the pyrgeometers at the beginning of the Phase I tests. Thus, no reliable long-wave radiation data were collected until the fourth week. At the end of the Phase I test series, all of the actinometers were turned face up for a quality control check. The pyranometers agreed to within 1 percent of each other, while the pyrgeometers were within 3 percent. The actinometers were sent to the White Sands Missile Range calibration facility for calibration between Phases I and II. Unfortunately, one of the pyrgeometers was damaged during return shipment and was unavailable during Phase II. In order to compensate for the missing pyrgeometer, incident longwave radiation was derived empirically using Brunt's formula (Kondratyev, 1969). The procedure was similar to the one used by Morgan et al. (1970) in radiation tests at Davis, California.

At the conclusion of Phase II the remaining pyrgeometer was turned face-up for 2 days to allow comparison of the measured incident long-wave radiation with the calculated radiation. The linear correlation coefficient between measured and calculated radiation for Day 1, which had clear skies during the entire day, was 0.96 and the mean values agreed to within 2 percent. Day 2 was partly cloudy, and the calculated radiation required an adjustment as suggested by Sellers (1965). After this adjustment, the correlation coefficient was 0.97. The means of the calculated radiation were within 1 percent of the measured values for Day 2. Because of these favorable comparisons, the empirical values for incident long-wave radiation were used to replace the missing pyrgeometer data for net radiation computation.

In an attempt to obtain Phase I flux measurements, a three-axis Applied Technologies, Inc. (ATI) sonic anemometer was mounted at the 2-m level on the Base Weather Station 10-m tower. This instrument is capable of measuring the alongwind, crosswind, and vertical wind components and temperature for flux measurements. The sonic anemometer produced questionable data throughout Phase I. At times the resultant wind speed and direction agreed well with the tower data, while at other times the correspondence was poor. The vertical (w) wind component on the sonic anemometer also contained a persistent bias, suggesting that the instrument was not adequately leveled. Consequently, data from this instrument were not used in the analysis.

One of the objectives of Phase II was to evaluate the relationships between the refractive index structure parameter C_N^2 and the measured sensible and latent heat fluxes. Sensible and latent heat fluxes can be calculated from the covariances of the fluctuations of the vertical wind speed (w') component with the fluctuations of the temperature (T') and absolute humidity (q'). These variables were measured during Phase II using single-axis sonic anemometers with fine-wire thermocouples (Model CA27T) and Krypton hygrometers (Model KH20) (see Tanner et al., 1985). Four flux measurement systems were set up, three at a height of 3.5 m AGL and one at 1.5 m AGL (Figure 4).



Figure 4. Flux Measurement Systems.

Critical experimental design considerations include instrument exposure, separation distance, path averaging, and data rate. The instruments were set up facing towards the southeast, with the hygrometer probe set 10 cm back from and 10 cm to the east of the front edge of the sonic anemometer probe to minimize flow distortion. The fine-wire thermocouple probe was located 2 to 3 cm from the sonic path. Priestly and Hill (1985) state that sensor separation degrades the cospectrum at spatial wavelengths smaller than four times the sensor separation. Consequently, no attempt was made to evaluate cospectra at scales smaller than 50 cm. Path averaging limits the spatial resolution of the measurement system. While the spatial resolution of the thermocouple and hygrometer is on the order of a few centimeters, the system resolution is limited by the 10-cm sonic path length. A data rate of 10 Hz was found to be

compatible with the instrument separation distance, resolution, and measurement height.

2.3 RELATIONSHIP OF C_N^2 TO OTHER ATMOSPHERIC VARIABLES

Over the last several decades a number of studies have related C_N^2 to the fluxes of heat and humidity. Coulter and Wesely (1980) derived the empirical relationship

$$H_s = 0.48z\gamma\rho c_p(g/T)^{1/2}[C_N T^2/(AP)]^{3/2} \quad (2-1)$$

where H_s is a derived heat flux, C_N is the square root of C_N^2 , ρ is air density, c_p is specific heat, T is the mean temperature, A is a wavelength-dependent refractive index coefficient, P is the atmospheric pressure, z is height above the surface, and γ is a water vapor correction term. Equation (2-1) is strictly valid only for optical wavelengths in quasi-steady-state, convectively unstable conditions such as found at midday. At wavelengths in excess of 1 μm and optical paths above warm, wet surfaces, water vapor pressure fluctuations become significant and sometimes emerge as the dominant contributors to C_N^2 . Wesely (1976) consolidated the relationship between C_N^2 and the fluctuations of temperature and humidity into the expression

$$C_N^2 = (C_T^2 A^2 P^2 / T^4) \left[1 + r_{Tq} \left(\frac{0.0626}{B} \right) + \left(\frac{0.0313}{B} \right)^2 \right] \quad (2-2)$$

where C_T^2 is the temperature structure parameter, B is the Bowen ratio (the ratio of sensible to latent heat fluxes) and r_{Tq} is the temperature-humidity cross-structure correlation coefficient, given by

$$r_{Tq} = C_{Tq} / C_T C_q \quad (2-3)$$

Equation (2-2) accounts for the combined temperature and humidity effects on C_N^2 . These effects vary as a function of the covariances $w'T'$, $w'q'$, and $T'q'$, where $w'T'$ (K m s^{-1}) and $w'q'$ ($\text{g m}^{-2} \text{s}^{-1}$) determine respectively the temperature and humidity fluxes, and $T'q'$ (K g m^{-3}) is the temperature-

humidity covariance. Hill et al. (1980) found the pressure fluctuation term to be several orders of magnitude less than the temperature and humidity terms. Consequently, the contribution of the pressure fluctuation term is ignored in Equation (2-2).

A divergence of opinion exists concerning the magnitude of r_{Tq} . The temperature-humidity cross-structure correlation is dependent on the coherence between T and q at the wavelengths of turbulence that cause the scattering that produces scintillation. Wesely and Hicks (1978) and Coulter and Wesely (1980) suggest that, at the small spatial scales of refractive inhomogeneities associated with the scattering of light, this coherence approaches zero. On the other hand, Priestley and Hill (1985) conclude from their measurement program that T and q are highly correlated at these scales, leading to an r_{Tq} near unity. Gossard and Sengupta (1988) define a homogeneous, steady-state model in which horizontal gradients of variance and covariance can be neglected, which allows r_{Tq} to approach unity under ideal atmospheric conditions. The results of the current study indicate that the coherence between T and q is very sensitive to departures from these ideal conditions.

The turbulence scale that causes scintillation response in a scintillometer is on the order of $(\lambda\Lambda)^{0.5}$, where λ is the scintillometer operating wavelength and Λ is the path length. For an optical scintillometer operating at a wavelength of 1 μm or less over a 1000 m path, the turbulence scale is on the order of several centimeters. This turbulence scale is on the lower end of the inertial subrange and very near the dissipation range of the spectrum where turbulent motion is dissipated into heat. A scintillometer operating at a wavelength of 1 cm over the same path uses turbulence scales on the order of 3 m. Near the surface, this turbulence scale is likely to be in the energy-containing portion of the spectrum where turbulence is not isotropic and varying degrees of correlation exist between w, T, and q. This subject is further addressed in Subsection 2.4.

C_q^2 , C_T^2 , and C_{Tq} are related through similarity concepts to the vertical fluxes of heat and humidity. Free convection relations defined by Kohsieck (1982) for the unstable surface layer are

$$w'T' = 0.55z(g/T)^{1/2}(C_T^2)^{3/4} \quad (2-5)$$

and

$$w'q' = 0.6z(g/T)^{1/2}(C_T^2)^{1/4}(C_q^2)^{1/2} \quad (2-6)$$

Kohsiek (1982) uses r_{Tq} to relate C_{Tq} to C_T^2 and C_q^2 . Kohsiek also offers a third estimate of the r_{Tq} magnitude as

$$r_{Tq} = C_{Tq}/(C_T^2)^{1/2}(C_q^2)^{1/2} \approx 0.75 \quad (2-7)$$

Relationships between fluxes and structure parameters are defined for stable atmospheric conditions using the Obukhov length L and temperature scaling factor T_* . The relationship derived for slightly stable conditions by Wyngaard et al. (1971) is

$$C_T^2 = (T_*^2/z^{2/3})[4.9(1 + 2.75(z/L))] \quad (2-8)$$

where T_* is the ratio of temperature flux $w'T'$ to friction velocity u_* and L is defined by

$$L = -u_*^3 T / (kgw'T') \quad (2-9)$$

where k is the Von Karman constant. Nocturnal conditions at DPG are characterized by clear skies, light winds, and extremely stable thermal stratification. These conditions violate assumptions used to develop T_* , u_* , and z/L relationships. It is, therefore, unrealistic to expect Equation (2-8) to define nocturnal C_T^2 with great precision.

Accurate measurements of u_* using eddy correlation techniques are difficult to obtain. Therefore, the relationship between u_* and σ_w , the square root of the variance in vertical wind speed, is used. Kondo et al. (1978) found that in stable conditions σ_w/u_* decreases from its neutral value of 1.3, reaching a plateau at 1.1 until the dimensionless stability parameter z/L exceeds 2.0. For z/L greater than 2.0, σ_w/u_* decreases rapidly until it stabilizes near a value of 0.5. As a first approximation,

$$u_* \approx \tilde{\sigma}_w / 1.1 \quad (2-10)$$

offers values of u_* for the stability range of interest in this study.

2.4 DATA SCREENING AND ANALYSES

Data from four closely spaced sets of fast-response (10-Hz) wind, temperature, and humidity sensors were used in the Phase II portion of the study. Data from these instruments were subjected to several stages of screening prior to analysis. For preliminary screening, raw data were subjected to an outlier check wherein data points more than three standard deviations from the mean were flagged. Very few data points were flagged using this procedure, indicating that the data did not contain many large noise spikes. The data were then divided into 18-min blocks for further reduction and analysis using the FLXVAR program, which calculates variances and covariances, and the RAWSPC program, which calculates spectra and cross spectra. These programs permit detailed data analyses and intercomparisons and provide the variables used to compute refractive index structure parameters. Some data sets were eliminated from further analysis because of temperature drift in the sonic anemometer reference temperature junction. This screening procedure left 16 trials of 18-min duration for further analysis. Each data set was further reduced by selecting only data from instruments on Masts 2 and 3 for detailed analysis. These instruments were adjacent (6-m separation) and mounted at the same elevation (3.5 m AGL).

Table 1 presents the variances computed for vertical velocity ($w'w'$), temperature ($T'T'$), and humidity ($q'q'$). The vertical velocity and temperature variances at Masts 2 and 3 remain consistent with each other for diurnal variations that range over several orders of magnitude. The humidity variance is uniformly small due to the dry ground conditions 10 days after the last major rainfall. Comparison of the humidity variances for the hygrometers on Masts 2 and 3 also reveals a measurement bias, with the magnitudes of the Mast 3 humidity variances approximately $0.0175 \text{ g}^2 \text{ m}^{-6}$ greater than those of Mast 2. Analysis of the spectra for data from these instruments revealed a large noise component on Mast 3 at the high frequency end of the measured spectra, and the

Mast 3 humidity variance bias is thought to be due to this noise. The noise effects did not appear in covariances because the random noise signal is uncorrelated with temperature and vertical velocity.

Table 1. Variances of Vertical Velocity ($w'w'$), Temperature ($T'T'$), and Humidity ($q'q'$).

Trial	Date (1988)	Start Time (MDT)	Mast 2 $w'w'$ ($m^2 s^{-2}$)	Mast 3 $w'w'$ ($m^2 s^{-2}$)	Mast 2 $T'T'$ (K^2)	Mast 3 $T'T'$ (K^2)	Mast 2 $q'q'$ ($g^2 m^{-6}$)	Mast 3 $q'q'$ ($g^2 m^{-6}$)
1A	16 Aug	1105	.121	.133	.699	.525	.014	.027
1B	16 Aug	1124	.119	.144	.534	.610	.009	.027
1D	16 Aug	1159	.136	.152	.640	.642	.010	.029
2A	17 Aug	0356	.002	.002	.055	.059	.015	.033
2B	17 Aug	0415	.012	.012	.085	.074	.052	.062
2C	17 Aug	0435	.012	.010	.065	.070	.002	.022
3A	17 Aug	0621	.003	.003	.165	.166	.014	.033
3B	17 Aug	0640	.010	.010	.731	.762	.043	.063
4C	17 Aug	1240	.146	.142	.612	.580	.082	.098
4D	17 Aug	1259	.185	.186	.794	.759	.017	.033
5A	18 Aug	0421	.015	.012	.510	.504	.009	.025
5B	18 Aug	0440	.006	.006	.187	.172	.006	.025
6A	18 Aug	0631	.002	.002	.167	.158	.015	.034
6B	18 Aug	0650	.007	.006	.800	.693	.021	.035
6C	18 Aug	0710	.006	.005	.163	.156	.009	.028
7A	18 Aug	1101	.104	.121	.464	.566	.013	.036

The temperature and vertical velocity covariances at Masts 2 and 3 exhibited large positive values at midday and small negative values in the early morning hours. These results, which are shown in Table 2, are consistent in sign and magnitude with the results obtained in the 1968 Kansas Field Program (Izumi, 1971).

The covariances of humidity with vertical velocity were uniformly positive, indicating continued evaporation from the ground surface following 10 days of intense heating after the last recorded precipitation. The covariances measured at night and during the transition at sunrise were characterized by occasional bursts of flux interspersed with quiescent periods of very low turbulence. Covariances during these periods, which were two or three orders of magnitude below midday covariances, were so small that they could have been influenced by neglected secondary effects such as advection. Consequently, they were assigned a magnitude of 0.000 in Table 2.

The data in Table 2 were used to compute the Bowen ratio, the ratio of sensible to latent heat flux densities, using the expression

$$B = \frac{c_p P(w'T')}{\epsilon L_w (w'e')} \quad (2-11)$$

where ϵ is the ratio of the molecular weights of water vapor to dry air, L_w is the latent heat of vaporization, and $w'e'$ is the humidity flux in units of millibar meters per second (mb m s^{-1}). Vapor pressure e in millibars is related to absolute humidity q in grams per cubic meter and air temperature T in degrees Kelvin by

$$e = \frac{qT}{216.7} \quad (2-12)$$

Table 3 summarizes the Bowen ratios calculated using Equation (2-11). The Bowen ratios B for the daytime trials range between 1 and 10, indicating a strong positive (upward) heat flux and a weak upward humidity flux above strongly heated dry ground. At night, B changes sign due to the downward heat flux. The smaller heat flux at night occasionally caused the absolute value of B to be slightly less than 1.0. For those cases shown in Table 3 in which

Table 2. Covariances of Vertical Velocity and Temperature ($w'T'$), Vertical Velocity and Humidity ($w'q'$), and Temperature and Humidity ($T'q'$).

Trial	Date	Start Time (1988)	Start	Mast 2	Mast 3	Mast 2	Mast 3	Mast 2	Mast 3
			MDT	$w'T'$ ($K \text{ m s}^{-1}$)	$w'T'$ ($K \text{ m s}^{-1}$)	$w'q'$ ($g \text{ m}^{-2} \text{ s}^{-1}$)	$w'q'$ ($g \text{ m}^{-2} \text{ s}^{-1}$)	$T'q'$ ($K \text{ g m}^{-3}$)	$T'q'$ ($K \text{ g m}^{-3}$)
1A	16 Aug	1105	.156	.115	.018	.015	.087	.066	
1B	16 Aug	1124	.134	.150	.013	.016	.057	.069	
1D	16 Aug	1159	.159	.164	.016	.018	.057	.064	
2A	17 Aug	0356	-.001	.000	.000	.000	-.006	-.006	
2B	17 Aug	0415	-.006	-.006	.003	.002	-.040	-.035	
2C	17 Aug	0435	-.005	-.005	.000	.000	-.002	-.002	
3A	17 Aug	0621	-.004	-.003	.001	.002	-.030	-.033	
3B	17 Aug	0640	-.010	-.014	.003	.004	-.149	-.156	
4C	17 Aug	1240	.139	.120	.011	.013	.062	.063	
4D	17 Aug	1259	.176	.156	.025	.024	.086	.091	
5A	18 Aug	0421	-.030	-.015	.004	.003	-.048	-.055	
5B	18 Aug	0440	-.007	-.006	.002	.000	-.017	-.015	
6A	18 Aug	0631	-.001	.001	.000	.000	-.044	-.044	
6B	18 Aug	0650	-.012	-.002	.002	.000	-.115	-.106	
6C	18 Aug	0710	-.003	.000	.000	.000	-.016	-.018	
7A	18 Aug	1101	.110	.116	.016	.027	.056	.083	

the humidity flux and B are missing, the humidity flux was below measurement resolution. It is reasonable to assume in these cases that B is a large number of undetermined sign. As a first-order approximation, the effects of humidity as represented by B in the denominator of the moisture contribution terms of Equation (2-2) can be neglected over strongly heated dry ground during summer months at DPG.

Before calculating C_N^2 , it is necessary to define the energy containing frequencies in the data and determine the magnitude of the temperature-humidity cross-structure correlation coefficient r_{Tq} . This parameter is a

Table 3. Mean Wind Speeds (WS), Temperatures (T), Pressures (P), Latent Heats of Vaporization (L_w), Humidity Fluxes ($w'e'$), and Bowen Ratios.

Trial	Date	Time	Start			L_w (cal g^{-1})	$w'e'$ (mb m s^{-1})	$w'e'$ (mb m s^{-1})	Bowen Ratio	
			WS (1988) (m s^{-1})	T (MDT) ($^{\circ}\text{C}$)	P (mb)				Mast 2	Mast 3
1A	16 Aug	1105	3.0	25.4	869.5	583	.026	.021	3.5	3.2
1B	16 Aug	1124	3.0	26.0	869.5	583	.018	.023	4.3	3.7
1D	16 Aug	1159	2.6	27.0	869.4	582	.022	.025	4.2	3.8
2A	17 Aug	0356	2.2	12.8	867.8	590	-- ^a	--	--	--
2B	17 Aug	0415	2.2	11.8	867.8	590	.004	.003	-0.9	-1.2
2C	17 Aug	0435	1.8	11.1	867.9	591	--	--	--	--
3A	17 Aug	0621	1.8	10.1	868.4	592	.002	.003	-1.2	-0.7
3B	17 Aug	0640	1.8	10.3	868.4	592	.004	.005	-1.4	-1.5
4C	17 Aug	1240	1.7	33.8	868.6	578	.016	.019	5.0	3.7
4D	17 Aug	1259	3.2	33.7	868.4	578	.036	.034	2.9	2.7
5A	18 Aug	0421	2.8	13.6	867.1	589	.005	.004	-3.7	-2.3
5B	18 Aug	0440	2.6	12.9	867.1	589	.002	--	-1.9	--
6A	18 Aug	0631	1.4	13.2	867.8	589	--	--	--	--
6B	18 Aug	0650	1.6	13.0	867.8	589	.002	--	-3.0	--
6C	18 Aug	0710	1.6	12.9	867.9	589	--	--	--	--
7A	18 Aug	1101	1.4	34.1	869.0	578	.023	.038	2.8	1.8

^a Humidity flux insignificantly different from zero.

function of scintillation wavelength, and is therefore a function of frequency. Spectrum analysis provides a breakdown by frequency band of contributions to the total variance in the data. Spectra of the vertical velocity, temperature, and humidity data for each trial were examined using the DPG spectrum analysis program described in Appendix B. The 10-Hz temperature and humidity data points were instantaneous readings and contained no averaging from higher frequency data. Therefore, the spectra contained energy aliased from the unsampled higher frequencies. To minimize these aliasing effects, 1-hr blocks of 10-Hz data were averaged over a frequency decade to 1-s intervals prior to analysis of the spectra. This averaging virtually eliminated aliasing effects that were evident in unaveraged 10-Hz data.

Spectral frequencies were converted to wavelength by dividing the trial-averaged 3.5-m windspeed by the central frequency of each spectral frequency band. Wind-speed measurements at 10 m were adjusted to 3.5 m using simple power-law relationships defined by Biltoft (1978). The wavelengths obtained for each of the 1-hr blocks of 1-Hz data ranged from several meters at the high frequency end of the spectrum to nearly 1000 m at the low frequency end.

Review of the spectra also served as an important quality control check to identify high frequency noise contamination independent of the aliasing problem. Unlike aliasing, the noise was not eliminated by averaging. High frequency noise was identified in the Mast 3 humidity data, which caused higher variances in this unit than those obtained from the other humidity instruments. Because this noise was uncorrelated with the temperature and vertical velocity data, the covariances presented in Table 2 remain unaffected.

Spectra of surface layer micrometeorological-scale atmospheric variables can be divided roughly into three regions (Kaimal, 1988): (a) the energy containing range, where energy is produced by buoyancy and shear; (b) the inertial subrange where energy is neither produced nor dissipated, but cascades progressively towards smaller scales; and (c) the dissipation range where kinetic energy is converted to internal energy through viscous dissipation. The portions of the spectra in the energy containing range include scales ranging in wavelength from meters to hundreds of meters. Covariances of variables in the energy containing range are primarily responsible for the fluxes of heat, momentum, and water vapor.

The inertial subrange includes scales ranging from a few millimeters to several meters. Within the convective surface boundary layer, the outer scale, or low frequency end of the inertial subrange, is approximately equal to the height above the surface. Energy within the inertial subrange is transferred in an essentially loss-free manner to progressively smaller scales and becomes partitioned more or less equally in all spatial dimensions. As this occurs, covariances between vertical motion and transported atmospheric constituents such as heat and water vapor diminish. Energy cascading down the

scales in the inertial subrange finally reaches the dissipation range, where viscous effects become dominant. At scales of a millimeter and below, random turbulent motions are converted into molecular motions or heat.

The maximum covariance between w , T , and q can occur when they vary over the same range of scale. Consequently, the vertical velocity, temperature, and humidity spectra were examined to determine the range of wavelengths for spectral maxima as a function of time of day. The ranges of spectral maxima for midday and nocturnal conditions are presented in Table 4. For trials conducted at midday, Table 4 shows that the spectral maxima for w , T , and q are of similar magnitude and are well within the energy containing region of the spectrum. Consequently, a relatively high degree of covariance was found, which results in large average flux values (see Table 5). At night, the wavelength scales of the spectral maxima for w are significantly smaller than the midday scales, while the spectral maxima for T and q occur at longer wavelengths. This decrease in the vertical motion scale is due less to a shift in spectral power peaks than to a differentially greater loss of power at the longer wavelengths. The shift of the w maximum toward the lower end of the energy containing range of the spectrum, and the attendant scale separation of spectral maxima is largely responsible for the smaller fluxes of heat and humidity during the night.

Table 4. Wavelength Ranges of Spectral Maxima For Vertical Velocity, Temperature, and Humidity.

Time of Day	Wavelength Range of Spectral Maximum (m)		
	Vertical Velocity w	Temperature T	Humidity q
Midday	10 - 300	20 - 300	30 - 300
Night	5 - 40	300 - 1000	250 - 1000

The averaged total heat and humidity fluxes and the flux contributions from the region of spectral maxima are shown in Table 5. Comparison of the

midday flux contribution from the spectral maximum with the total flux illustrates the large contribution from a rather narrow band within the energy containing region of the spectrum. At night and during the sunrise transition, the contributions to the total fluxes are smaller and more distributed.

Table 5. Total And Spectral Maxima For Heat ($w'T'$) And Humidity ($w'q'$) Fluxes.

Total ($W m^{-2}$)						Spectral Maxima ($W m^{-2}$)					
Day		Night		Sunrise		Day		Night		Sunrise	
$w'T'$	$w'q'$	$w'T'$	$w'q'$	$w'T'$	$w'q'$	$w'T'$	$w'q'$	$w'T'$	$w'q'$	$w'T'$	$w'q'$
142	45	-8	3	-5	3	48	15	-2	0.8	-0.5	0.7

The $w'T'$ and $w'q'$ fluxes indicate the movement of heat and humidity vertically through the atmosphere. The larger scale movements or fluxes generated within the energy containing range of the spectrum transport smaller scale scintillation-causing eddies across an optical path. Therefore, the flux summed across the entire energy containing range is the pertinent variable for $w'T'$ and $w'q'$ effects on C_N^2 . In contrast, the $T'q'$ covariance is pertinent only for the wavelength bands that affect the scintillation scales of interest. As discussed in Subsection 2.3, the wavelength bands of interest range from several millimeters to several centimeters for optical wavelength scintillation effects, and over several meters for mmw scintillation effects. Figures 5 and 6 show the wavelength-dependent correlation, or coherence, between combinations of w' , T' , and q' for summer midday (Trial 1) and nocturnal (Trial 2) conditions at DPG. Because of the averaging done to eliminate aliasing, coherence in Figures 5 and 6 does not extend to wavelengths much below 10 m. However, a trend towards decreasing coherence at shorter wavelengths is apparent in these Figures.

The $w'T'$ and $w'q'$ coherence is relatively high within the energy containing region of the spectrum during midday. This coherence is low at night due largely to the weakness of vertical motions within the energy containing region of the spectrum. There is also a trend for coherence to decrease at progressively smaller wavelengths within the inertial subrange due to random partitioning of turbulent energy.

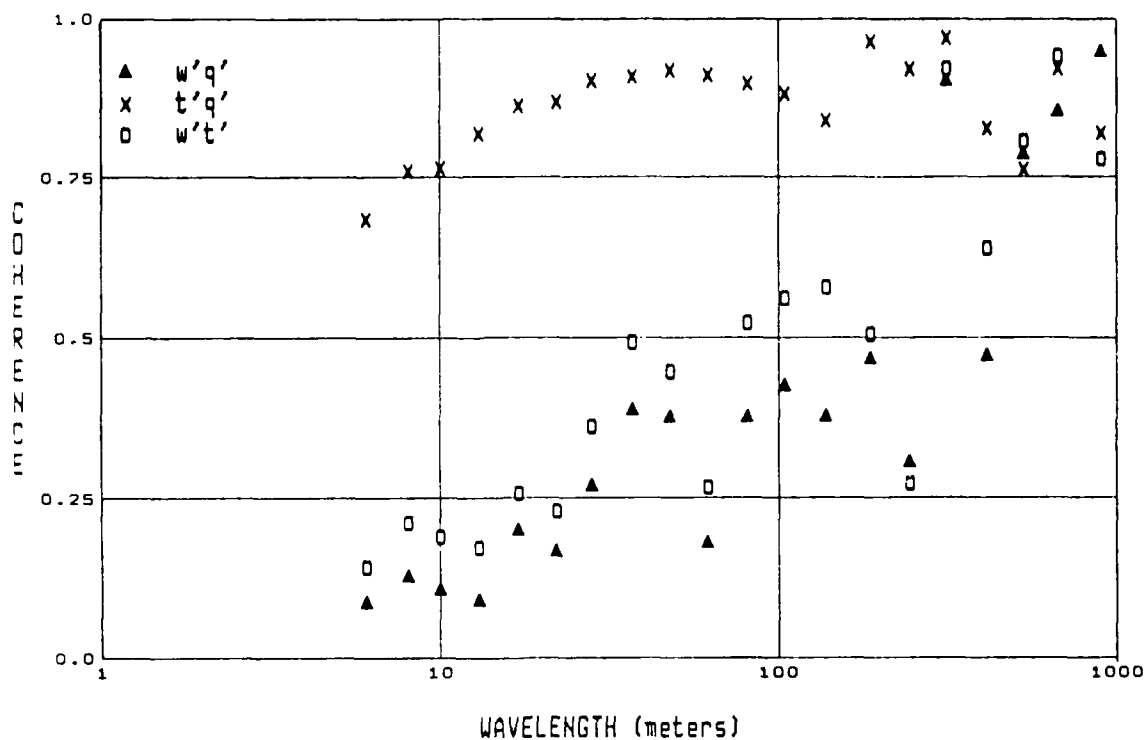


Figure 5. Coherence of w' to q' , T' to q' and w' to T' for Trial 1, Representing Midday Conditions During the Summer at DPG.

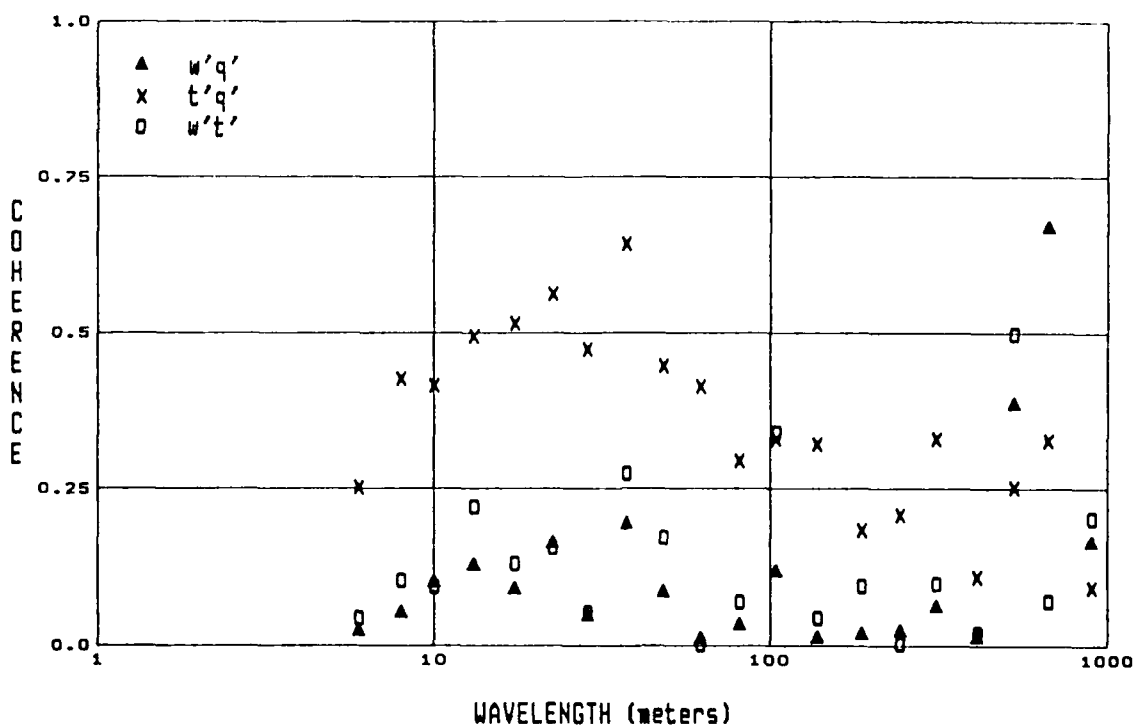


Figure 6. Coherence of w' to q' , T' to q' , and w' to T' for Trial 2, Representing Nocturnal Conditions During the Summer at DPG.

The midday $T'q'$ coherence shown in Figure 5 remains high for wavelengths in excess of 10 m, but decreases at shorter wavelengths. The nocturnal $T'q'$ coherence in Figure 6 remains low for all frequencies. Although the spectra do not extend to the centimeter scales to which optical scintillometers respond, trends in the available data suggest that coherence at these scales is closer to zero than to unity. These $T'q'$ coherence tendencies differ from the findings of Priestley and Hill (1985), who reported coherence of 0.8 or greater extending to wavelengths well below 1 m for measurements over moist soils.

Several possible explanations exist for the low $T'q'$ coherence in the DPG data. One possibility is an undetected deficiency in data collection or processing. However, the data reduction computer program used on the DPG data was derived from the one described by Kaimal and Gaynor (1983) and should be appropriate for use with these data. Also, the 10-Hz data were averaged to 1 Hz to eliminate aliasing, and these averaged data exhibited no obvious remnants of aliasing that would artificially degrade coherence.

Another possible explanation for the low $T'q'$ coherence in the DPG data lies within the physics of the problem. Neglecting molecular diffusion and assuming that a flux tends to be directed down the gradient (from the source towards a sink), high $T'q'$ coherence can occur if the ratio of moisture and heat gradients remains constant. Gossard and Sengupta (1988) represent this ratio as $(\partial q / \partial z) / (\partial \theta / \partial z)$, where θ is potential temperature. They conclude that this ratio is a conservative property over homogeneous terrain, causing high $T'q'$ coherence down to very small spatial scales. While the ratio of gradients for saturation vapor pressure to temperature $(\partial e_s / \partial z) / (\partial T / \partial z)$ is conservative, the actual vapor pressure or absolute humidity above the ground surface is influenced by factors such as percolation of moisture through the soil and variations in evapotranspiration rates. As long as sufficient moisture is available at the surface, the conclusion of Gossard and Sengupta (1988) remains approximately correct. However, as a surface becomes progressively drier, less moisture is available, and the parts of the surface that have been most strongly heated are likely to have the least available moisture. The result is a decrease in $T'q'$ coherence. Coherence should

approach zero when the moisture gradient vanishes above a desiccated surface. The lowest coherence (0.76) reported by Priestly and Hill (1985) occurred during their driest daytime test conditions, a result that is consistent with this analysis.

An additional complication occurs during measurements at night when a stable thermal stratification isolates the surface layer from layers several meters above it, eliminating convective transfer of heat and moisture. These upper layers of air are drifting randomly over the surface, mixing very little with layers above and below. Also, shifts in wind direction may cause instruments at a fixed location to sample air from several different origins over the course of a measurement period. Therefore, the $T'q'$ coherence for air sampled during dry nocturnal conditions is likely to have a large random component that differs significantly from unity, as demonstrated in Figure 6.

2.5 CALCULATION OF OPTICAL AND MILLIMETER-WAVE C_N^2 FROM FLUXES

Equation (2-2) can be used to compute optical C_N^2 from the fluxes of heat and moisture as measured by the fast-response instruments on Masts 2 and 3. Intermediate steps in this procedure, which include the estimation of the Bowen ratio and r_{Tq} , are discussed in Subsection 2.4. Estimates of C_T^2 and C_q^2 are obtained in this subsection using the method of Kohsiek (1982) for the unstable trials and the method of Wyngaard et al. (1971) for the stable trials. Because the trials conducted during the sunrise transition period generally had negative average heat fluxes, the method of Wyngaard (1971) was used for these trials as well.

The C_T^2 and C_q^2 values calculated using Equations (2-5) and (2-6) for the convectively unstable midday data found in Tables 2 and 3 are shown in Table 6. These data were computed for the 2-m level, assuming constant fluxes between 2 m and the 3.5-m measurement level. The relative magnitudes of the C_T^2 and C_q^2 values in Table 6 indicate the relative strengths of daytime heat and humidity fluxes over dry desert terrain. When presented in terms of Bowen ratio, the C_{Tq} contribution (represented by the term in Equation (2-2) containing r_{Tq}) contributes between 1 and 3 percent to the total optical C_N^2 .

if an r_{Tq} of 1.0 is assumed. Because r_{Tq} at optical wavelengths is likely to be closer to zero, this contribution becomes negligible. The C_q^2 contribution, represented by the $(.0313/B)^2$ term in Equation (2-2), is on the order of 0.01 percent, which is also negligible.

Table 6. Calculated Temperature (C_T^2) and Humidity (C_q^2) Structure Parameters for the Midday Trials.

Trial	Date (1988)	Start Time (MDT)	$C_T^2 \left[\frac{K^2}{m^{2/3}} \right]$		$C_q^2 \left[\frac{(g \ m^{-3})^2}{m^{2/3}} \right]$	
			Mast 2	Mast 3	Mast 2	Mast 3
1A	16 Aug	1105	.724	.480	.009	.007
1B	16 Aug	1124	.590	.683	.005	.007
1D	16 Aug	1159	.742	.772	.006	.008
4C	17 Aug	1240	.632	.519	.004	.005
4D	17 Aug	1259	.863	.734	.015	.015
7A	18 Aug	1101	.463	.499	.009	.022

The C_T^2 and C_q^2 values calculated for the nocturnal and stable transition period trials using Equation (2-8) are given in Table 7. Following Hill et al. (1988), C_q^2 was calculated by replacing T_* in Equation (2-8) with the humidity scaling factor q_* , which is the ratio of $w'q'$ to u_* . The use of Equation (2-8) required as initial steps the estimation of u_* from Equation (2-10) and the Obukhov length L from Equation (2-9). As in the case of Table 6, C_T^2 was computed for the 2-m level by assuming a constant flux between that level and the instrument height of 3.5 m. This assumption is not well founded for extremely stable conditions. The nocturnal C_T^2 in Table 7 are generally smaller than the daytime values in Table 6. Also, the differences between the C_T^2 calculated using data from Masts 2 and 3 are sometimes large, indicating the general lack of homogeneity in very stable nocturnal conditions. No computations were made using Mast 3 data for Trials 2A, 6A, and 6C because the signs of the heat fluxes for these periods were indeterminate.

Table 7. Friction Velocity (u_*), Obukhov Length (L), and Calculated Temperature (C_T^2) and Humidity (C_q^2) Structure Parameters for the Stable Trials.

Trial	Date (1988)	Start Time (MDT)	u_* ($m s^{-1}$)		L (m)		C_T^2 $\left[\frac{K^2}{m^{2/3}} \right]$		C_q^2 $\left[\frac{(g m^{-3})^2}{m^{2/3}} \right]$	
			Mast 2	Mast 3	Mast 2	Mast 3	Mast 2	Mast 3	Mast 2	Mast 3
2A	17 Aug	0356	.04	M ^a	7.2	M ^a	.002	M ^a	M ^a	M ^a
2B	17 Aug	0415	.10	.10	11.5	12.3	.018	.016	.005	.002
2C	17 Aug	0435	.10	.09	14.5	14.5	.011	.012	M ^a	M ^a
3A	17 Aug	0621	.05	.05	2.8	2.6	.049	.039	.006	.015
3B	17 Aug	0640	.09	.09	5.8	3.7	.065	.196	.006	.016
5A	18 Aug	0421	.11	.10	3.4	4.9	.585	.149	.008	.005
5B	18 Aug	0440	.07	.07	3.4	4.1	.087	.050	.005	M ^a
6A	18 Aug	0631	.04	M ^a	7.2	M ^a	.002	M ^a	M ^a	M ^a
6B	18 Aug	0650	.07	.07	2.5	11.3	.266	.005	.005	M ^a
6C	18 Aug	0650	.07	M ^a	8.1	M ^a	.008	M ^a	M ^a	M ^a

^a Data Unavailable.

Table 8 compares the C_N^2 values calculated using Equation (2-2) with the values measured by the optical scintillometer. The calculated C_N^2 values in this table vary according to the multiplication factor ($A^2 P^2 / T^4$), which represents the sensitivity of the refractive index for the optical wavelengths to the average pressure and temperature. The multiplication factors are included in Table 8. Most of the C_N^2 values computed for the midday trials are within ± 30 percent of the observed values. This degree of correspondence is indicative of a well mixed atmosphere. Although the C_N^2 values for some of the nocturnal and transition trials agree well with the observed values, others are considerably different. This hit-or-miss condition is likely due to localized differences in C_N^2 that occur during nocturnal stratification and intermittent

turbulence conditions. The overall precision, defined as the standard deviation of the differences between observed and measured C_N^2 values for all trials, is about an order of magnitude. This result is strongly influenced by one calculated C_N^2 (Trial 5A, Mast 2) that diverged widely from the measured C_N^2 . For the nocturnal and transition trials, the precision of the C_N^2 calculated using the Mast 2 and Mast 3 data was roughly comparable to the precision obtained when the C_N^2 calculated using data from either mast are compared to the measured C_N^2 , further illustrating the effects of localized variations on C_N^2 .

Table 8. Multiplication Factor and Calculated and Measured Optical Refractive Index Structure Parameters.^a

Trial	Date (1988)	Start Time (MDT)	Multiplication Factor ($A^2 P^2 / T^4$)	Calculated C_N^2		Measured C_N^2
				Mast 2	Mast 3	
1A	16 Aug	1105	57.76	41.8	27.7	50.6
1B	16 Aug	1124	57.76	34.1	39.5	56.2
1D	16 Aug	1159	56.25	41.7	43.4	59.4
2A	17 Aug	0356	68.89	0.1	M ^b	4.1
2B	17 Aug	0415	70.56	1.3	1.1	2.2
2C	17 Aug	0435	70.56	0.8	0.8	1.9
3A	17 Aug	0621	72.25	3.5	2.8	5.7
3B	17 Aug	0640	72.25	4.7	14.2	6.0
4C	17 Aug	1240	51.84	32.8	26.9	34.7
4D	17 Aug	1259	51.84	44.7	38.1	41.2
5A	18 Aug	0421	67.24	39.3	10.0	6.4
5B	18 Aug	0440	68.89	6.0	3.4	4.3
6A	18 Aug	0631	68.89	0.1	M ^b	2.6
6B	18 Aug	0650	68.89	18.3	0.4	7.5
6C	18 Aug	0710	68.89	0.6	M ^b	2.3
7A	18 Aug	1101	51.84	24.0	25.8	26.8

^a Units for the multiplication factor are $K^{-2} \times 10^{-14}$ and for C_N^2 are $m^{-2/3} \times 10^{-14}$.

^b Data unavailable.

At infrared through millimeter wavelengths, absorption and refraction caused by water vapor become the dominant contributors to C_N^2 . Analytic applications appropriate for infrared and mmw propagation are credited to Hill et al. (1980) and Hill and Clifford (1981). Neglecting secondary effects by other atmospheric constituents (carbon dioxide, ozone, aerosols), they derived expressions for the log amplitude variance of infrared through mmw radiation propagation as functions of C_T^2 , C_q^2 , and C_{Tq} . The real component of the refractive index for a propagating spherical wavefront is (Hill et al, 1980)

$$C_N^2 = \frac{A_T^2 C_T^2}{T^2} + \frac{A_q^2 C_q^2}{q^2} + \frac{2 A_T A_q C_{Tq}}{Tq} \quad (2-13)$$

where A_T and A_q are frequency-dependent dimensionless sensitivity coefficients that account for changes in refractivity and absorption due to temperature and humidity fluctuations. McMillan et al (1983) define A_T and A_q for mmw propagation as

$$A_T = - \left(\frac{77.6P}{T} + \frac{1710q}{T} \right) \times 10^{-6} \quad (2-14)$$

and

$$A_q = \left(\frac{1710q}{T} \right) \times 10^{-6} \quad (2-15)$$

where P is in millibars, q is in grams per cubic meter, and T is in degrees Kelvin. For the temperature-humidity cross-structure, Hill et al (1988) suggest that r_{Tq} is unity. Under this assumption, Equation (2-3) shows that C_{Tq} can be obtained from

$$C_{Tq} = \pm \sqrt{C_T^2 C_q^2} \quad (2-16)$$

A detailed justification for this assumption is provided in Hill et al. (1988). The Equation (2-13) components for mmw C_N^2 derived from DPG data are presented in Table 9. In deriving these components, C_T^2 and C_q^2 were obtained from Tables 6 and 7, and C_{Tq} was calculated using Equation (2-16).

Comparison of the mmw C_N^2 components in Table 9 with each other and with the optical wavelength C_N^2 provided in Table 8 illustrates the importance of humidity fluctuations in desert terrain. The temperature structure term (containing C_T^2) in Table 9 is comparable in magnitude to the optical C_N^2 in Table 8, which is due almost entirely to C_T^2 effects. However, the humidity structure and humidity-temperature cross-structure terms also make significant contributions to mmw C_N^2 . The sign of the cross-structure term is negative during midday trials because the sign of A_T is negative and the sign of C_{Tq} is taken from r_{Tq} , which is positive during midday. In most cases, the cross-structure term is nearly equal in magnitude to the sum of the temperature and humidity structure terms. Therefore, if r_{Tq} is unity, the results in Table 9 indicate that mmw C_N^2 is much smaller than optical C_N^2 during the day and much larger than optical C_N^2 at night. For comparison, the magnitudes of mmw C_N^2 with r_{Tq} of zero and unity are presented in Table 9. The diurnal variation of mmw C_N^2 appears to be much more reasonable under the assumption of r_{Tq} equal to zero. As noted in Subsection 2.4, DPG coherence data suggest that r_{Tq} equal to zero is the better approximation at DPG. Direct mmw C_N^2 measurements were not available to verify the calculated C_N^2 in Table 9.

2.6 COMPARISONS OF ACTINOMETER AND SCINTILLOMETER DATA

The purposes of Phase I of this study, the demonstration or feasibility phase, were to: (a) obtain concurrent radiation and C_N^2 data over a typical wintertime snow surface and (b) develop data reduction and display routines. Phase I was originally scheduled to begin on 16 February 1988 and last for 2 weeks. One week before the planned start, DPG had a 7- to 10-cm snow cover. With temperatures forecasted to be above freezing, the snow cover was predicted to dissipate within a week. In order to make measurements over snow, the test was started a week early even though all of the instrumentation was not operational. Instrumentation problems occurred throughout Phase I, and

Table 9. Components of Equation (2-13) for Millimeter-Wave C_N^2 Computation.^a

Trial (1988)	Date	Start Time (MDT)	T (K)	T^q ($g \text{ m}^{-3}$)	Mast 2	Mast 3	C_N^2		
							$A_T^2 C_T^2$		$A_q^2 C_q^2$
							T^2	q^2	Tq
1A	16 Aug	1105	298.6	4.0	50.29	33.34	29.52	22.96	-77.06 -55.33
1B	16 Aug	1124	299.2	4.0	40.47	46.85	16.33	22.86	-51.42 -65.46
1D	16 Aug	1159	300.2	4.0	50.21	52.24	19.47	25.96	-62.53 -73.65
2A	17 Aug	0356	286.0	4.0	0.18	^b	^b	^b	^b ^b
2B	17 Aug	0415	285.0	4.0	1.50	1.29	16.82	7.78	10.03 6.33
2C	17 Aug	0435	284.3	4.0	0.88	1.03	^b	^b	^b ^b
3A	17 Aug	0621	283.3	4.0	4.03	3.25	23.24	54.06	19.35 26.52
3B	17 Aug	0640	283.5	4.0	5.42	16.35	23.63	57.92	22.62 61.53
4C	17 Aug	1240	307.0	4.0	38.68	31.76	12.41	15.51	-43.82 -44.39
4D	17 Aug	1259	306.9	4.0	52.86	44.96	46.57	46.57	-99.23 -91.51
5A	18 Aug	0421	286.8	4.0	46.25	11.81	28.44	19.14	72.54 30.07
5B	18 Aug	0440	286.1	4.0	6.97	3.97	17.27	^b	21.94 ^b
6A	18 Aug	0631	286.4	4.0	0.09	^b	^b	^b	^b ^b
6B	18 Aug	0650	286.2	4.0	21.33	0.43	18.38	^b	39.60 ^b
6C	18 Aug	0710	286.1	4.0	0.70	^b	^b	^b	^b ^b
7A	18 Aug	1101	307.3	3.8	28.38	30.58	27.87	68.12	-56.24 -91.29

^aUnits for Equation (2-13) components are $\text{m}^{-2/3} \times 10^{-14}$.

^bData unavailable.

the test was extended to 4 weeks in order to collect data from most of the instruments. The scintillometer produced valid data during the first week and part of the second. During the rest of Phase I, the scintillometer operated intermittently because of a series of problems such as failure of the LED in the transmitter.

An analysis of relationships between available Phase I scintillometer C_N^2 and actinometer radiation data was performed on several data sets. One 2-day data set was collected during the first week (10 and 11 February 1988). Temperatures on both days ranged from 7 °C during the day to -7 °C at night. Also, skies on both days were cloudy early in the day and then decreased throughout the day. Winds were strong ($5-20 \text{ m s}^{-1}$) from the northwest for much of 10 February and light and variable on 11 February. Snow cover was 10.2 cm on the morning of 10 February, decreasing to 2.5 cm by the afternoon of 11 February.

Solar radiation and C_N^2 measurements for 10 and 11 February 1988 are shown in Figures 7 and 8, respectively. As expected, the incident short-wave radiation on 10 February rises steadily to a peak around solar noon and then decreases. The few dips in the radiation curve represent periods of cloudiness. The scintillometer C_N^2 values remain steady throughout the day and then start to decrease about 3-4 hr after sunset. C_N^2 readings remain low during the night and then start to rise again about 1 hr after sunrise. Little relationship was found between C_N^2 and incident short-wave radiation during the daytime on 10 February. In contrast, on 11 February the C_N^2 readings tracked with changes in solar radiation (Figure 8). There are two main meteorological differences between these days: (a) the 10.2-cm snow cover of 10 February had almost dissipated by 11 February and (b) the wind speed was much greater on 10 February.

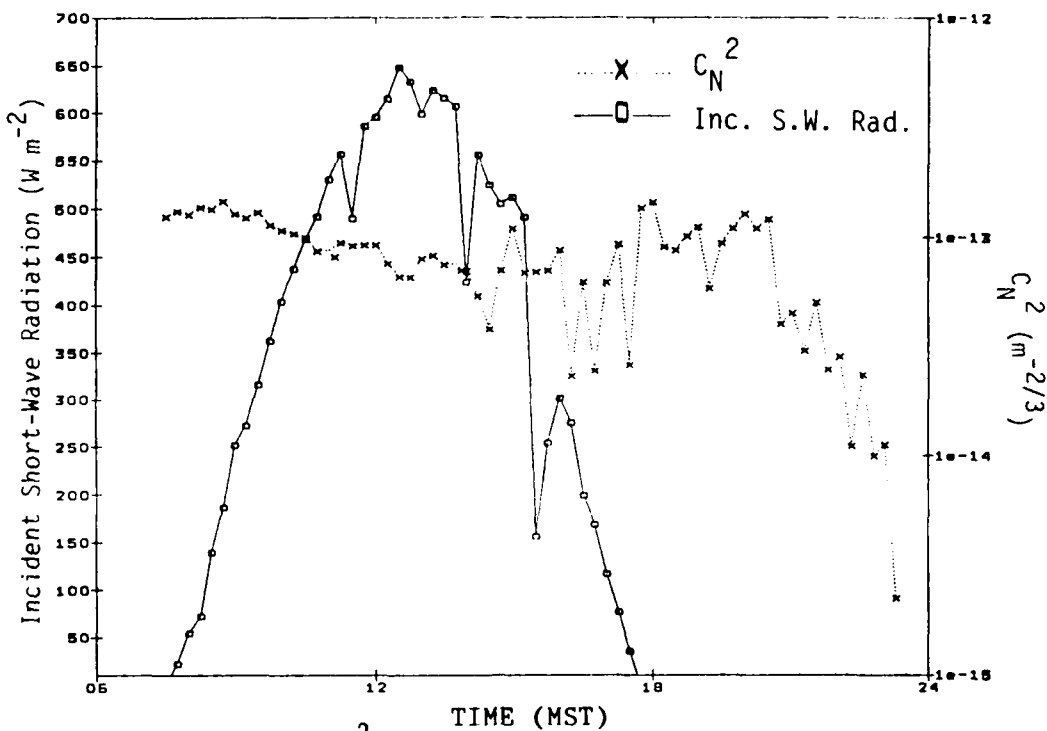


Figure 7. Scintillometer C_N^2 and Incident Short-Wave Radiation Data for 10 February 1988.

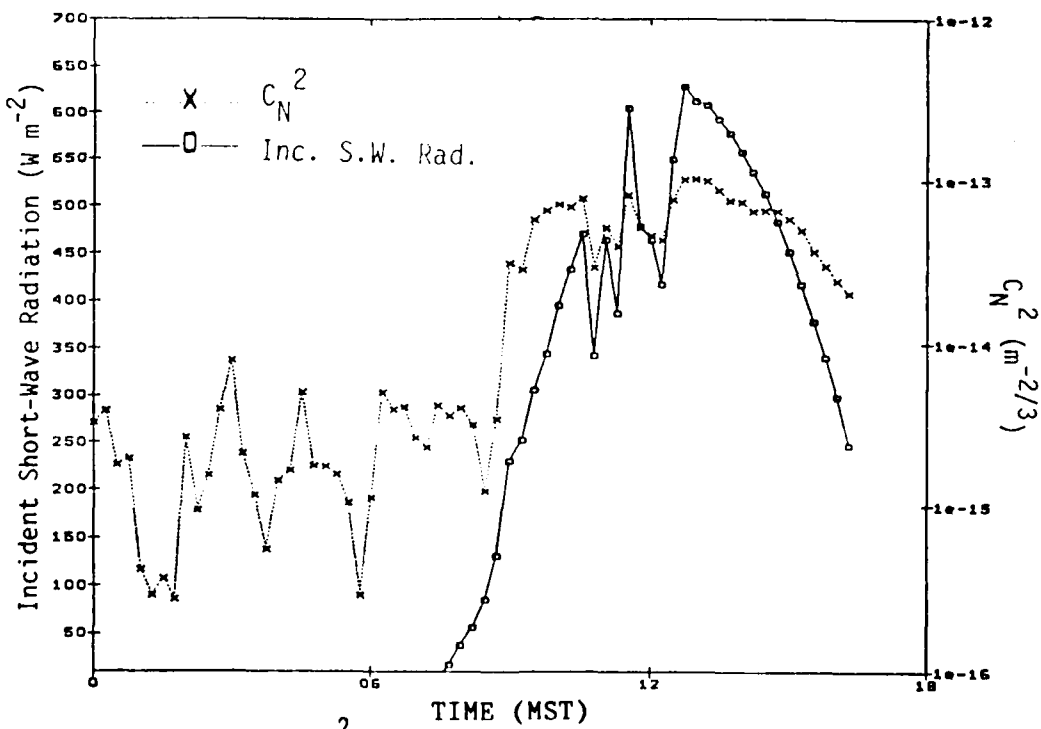


Figure 8. Scintillometer C_N^2 and Incident Short-Wave Radiation Data for 11 February 1988.

An interesting Phase I case occurred on 16 February. This day was cloudy and windy, with intermittent snow pellets between 1200-1600 Mountain Standard Time (MST). Figure 9 shows unusually high C_N^2 values ($10^{-12} \text{ m}^{-2/3}$) between 1200-1600 MST, which possibly are attributable to the precipitation. One possible explanation for the high measured C_N^2 values is a signal reflected from the snow pellets. Another possible explanation is vibration induced on the scintillometer receiver as it was struck by the snow pellets. Figure 9 indicates that, while the C_N^2 values peaked during precipitation, the incident short-wave radiation curve dipped. When the precipitation stopped, C_N^2 returned to normal levels and the radiation curve rose. This result suggests that further testing may be needed to determine the effects of various types and intensities of precipitation on scintillometer C_N^2 measurements.

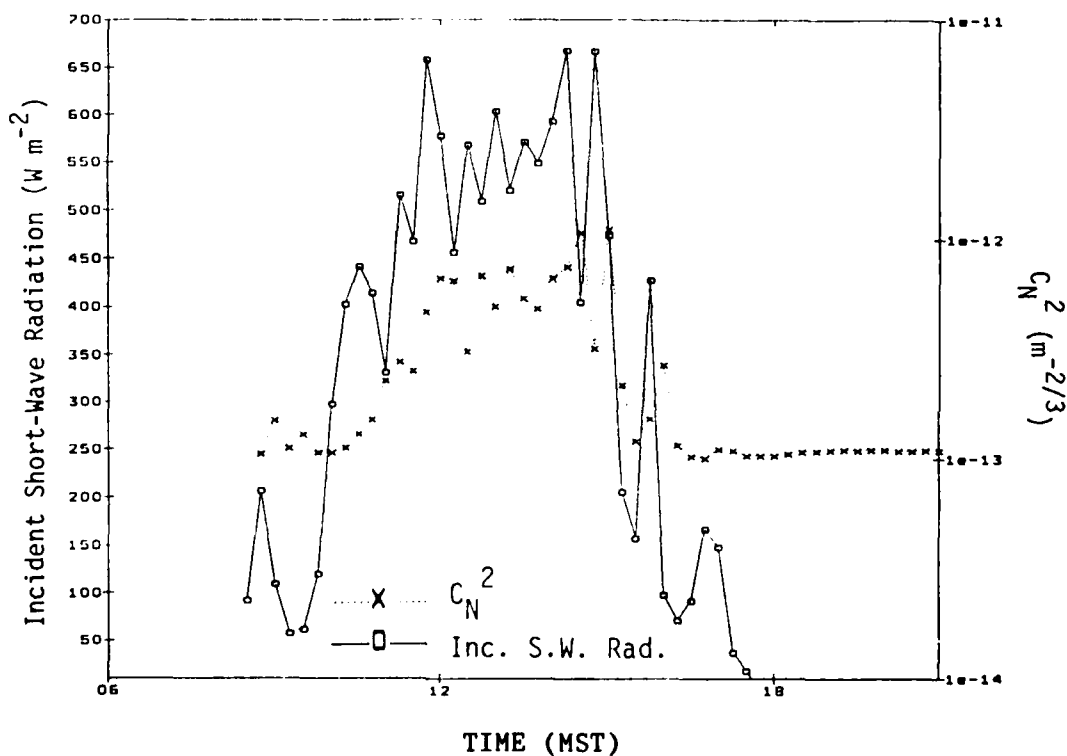


Figure 9. Scintillometer C_N^2 and Incident Short-Wave Radiation Data for 16 February 1988.

Figure 9 also illustrates a problem that began at approximately 1700 MST on 16 February 1988 when the scintillometer began to give a constant C_N^2 reading of

$10^{-13} \text{ m}^{-2/3}$. A low voltage on the transmitter was found when the instrument was checked the following day.

The Phase I objectives of demonstrating the measurement capability and developing data reduction and display routines were partly met. All of the instruments designated for the Phase I test were deployed and data were collected from them. The lessons learned during Phase I were helpful in designing the August Phase II trials. Data reduction and display routines were developed which made data interpretation easier. A computer program was written to convert scintillometer C_N^2 data from mV to the commonly used units of $\text{m}^{-2/3}$. Another program was developed to calculate net radiation from the four actinometers. A computer graphics package was selected to produce graphs for analysis.

There were several days during Phase I with good C_N^2 and incident short-wave radiation measurements, which allowed comparisons to be made. These measurements did not correspond well when there was snow covering the ground. However, there was only one day during Phase I with the desired snow cover. More extensive measurements during the wintertime with snow cover are needed to define any relationships between C_N^2 and other meteorological variables during that time of the year. Better correspondence between C_N^2 and incident short-wave radiation was found on Phase I days with no snow cover. Because these data showed promise for a relationship between C_N^2 and radiation, this possibility was further explored during Phase II.

The scintillometer was operated continuously during Phase II and performed well with no problems. Comparisons between Phase II scintillometer and actinometer data were made to further define a relationship between C_N^2 and radiation. Data were collected from 0930 Mountain Daylight Time (MDT) on 16 August to 1200 MDT on 18 August 1988. Fifteen-minute averages were used to obtain a workable data set, yet not smooth out fluctuations due to transient changes in cloud cover. Meteorological conditions on 16 and 17 August included clear skies and light and variable winds during the daylight hours. Light southeasterly drainage winds predominated between midnight and sunrise.

Temperatures ranged from 35 °C at midday to near 10 °C at night. A high, thin cloud cover advected over the test site after sunrise on 18 August.

Figure 10 shows the scintillometer C_N^2 data for 16-18 August 1988. Peak values of C_N^2 occur during the afternoon heating as extreme surface temperatures produce large density gradients. C_N^2 values reach minima during the transition periods when the atmosphere becomes quasi-adiabatic. Although the magnitude of C_N^2 momentarily drops below instrument threshold as transition occurs, the data from this event are averaged with the data obtained before the transition to produce a measurable 15-min reading. After the transition minimum at sunset, C_N^2 increases again during the nighttime as a thermal imbalance is produced by radiational cooling.

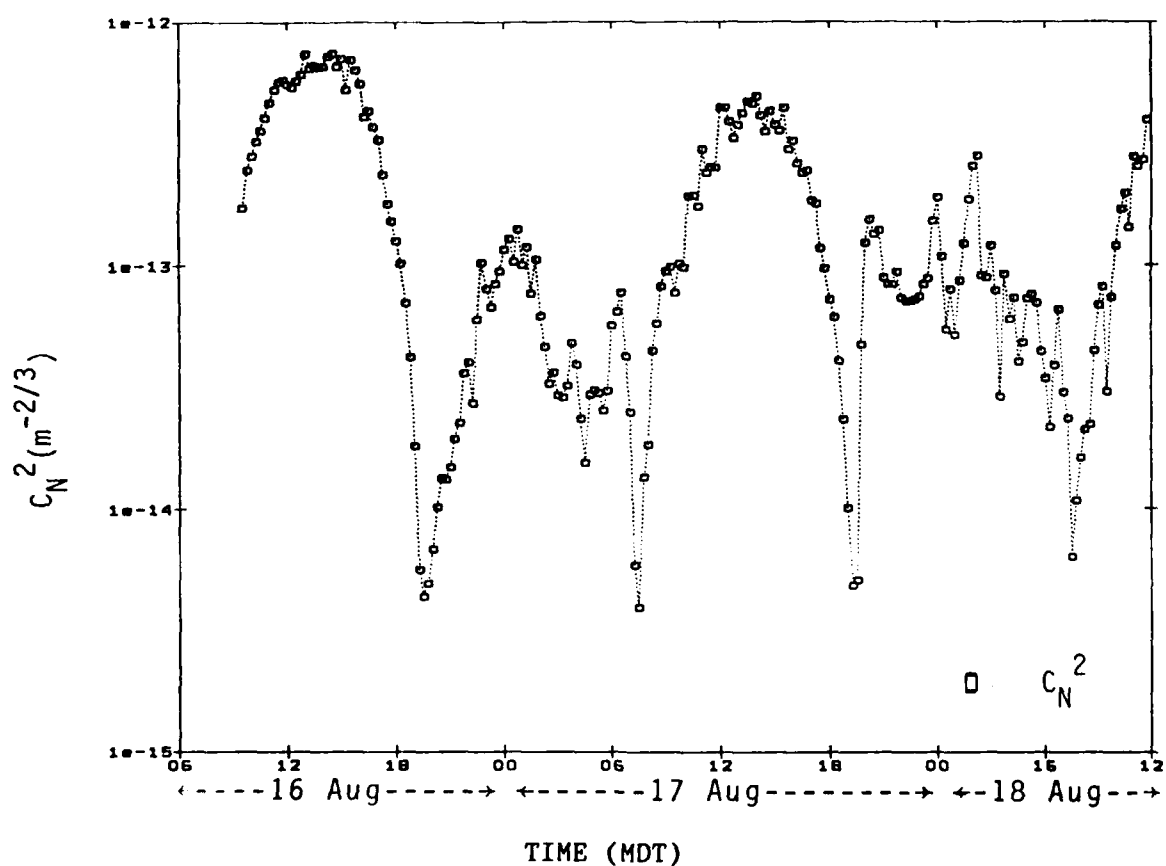


Figure 10. Scintillometer C_N^2 Record for 16 - 18 August 1988.

It should be noted that the transition period C_N^2 minima do not occur exactly at sunrise and sunset because of the thermal lag between the surface and air temperatures. The C_N^2 minima occur 15 to 30 min after sunrise and 1 hr before sunset. These results are similar to the results obtained by Walters and Kunkel (1980) at White Sands Missile Range (WSMR), where the C_N^2 minima were about 1.5 hr after sunrise and 0.5 hr before sunset. Various factors could contribute to the differences between DPG and WSMR, including soil type and height of measurement. (The measurement heights in the DPG and WSMR studies were 2 and 8 m, respectively.)

Three types of radiation (incident short-wave, emitted long-wave, and net) were compared with C_N^2 . Incident short-wave radiation versus C_N^2 for 16, 17, and 18 August is illustrated in Figure 11. As shown by the figure, the variations in C_N^2 closely track changes in incident short-wave radiation during the daytime.

Emitted long-wave radiation versus C_N^2 is shown in Figure 12. The best correspondence between the two is found during the daytime, although the correlations were not as high as found between C_N^2 and incident short-wave radiation. Similar analyses of the transition and nighttime data indicated no interrelationships between C_N^2 and long-wave radiation during transition periods and a low correlation at night.

The third radiation parameter compared with C_N^2 was net radiation. Net radiation was computed by first finding the net short-wave radiation and net long-wave radiation and then adding the two. Net short-wave is defined as incident short-wave radiation minus reflected short-wave radiation, while net long-wave radiation is defined as incident long-wave radiation minus emitted long-wave radiation. With the exception of the empirically derived incident long-wave radiation (see Subsection 2.2), all radiation values were measured with Eppley actinometers. As shown in Figure 13, the correspondence between C_N^2 and net radiation was again high during the daytime and not significant during the transition periods and at night. As noted earlier, 18 August was the only day during Phase II with some cloud cover. It is interesting to note the correspondence between dips in both the C_N^2 and incident short-wave radiation curves on this day, as shown in Figure 14 between 0900 and 1200 MDT.

These dips are periods when the clouds obscured the sun. Similar results were noted on partly cloudy days during Phase I.

In summary, both incident short-wave and net radiation are highly correlated with optical C_N^2 during the daytime hours of clear and cloudy days. These results are encouraging for our goal of establishing a C_N^2 climatology using available, continuously operated instrumentation. Unfortunately, results were not so good during the transition and nighttime phases, and it appears that another method will have to be found for these parts of the diurnal cycle. No Phase II testing was performed during periods with high winds or precipitation. In addition, Phase II data were collected over only a 3-day period. A longer testing period is needed under a variety of meteorological conditions in order to verify C_N^2 and radiation relationships.

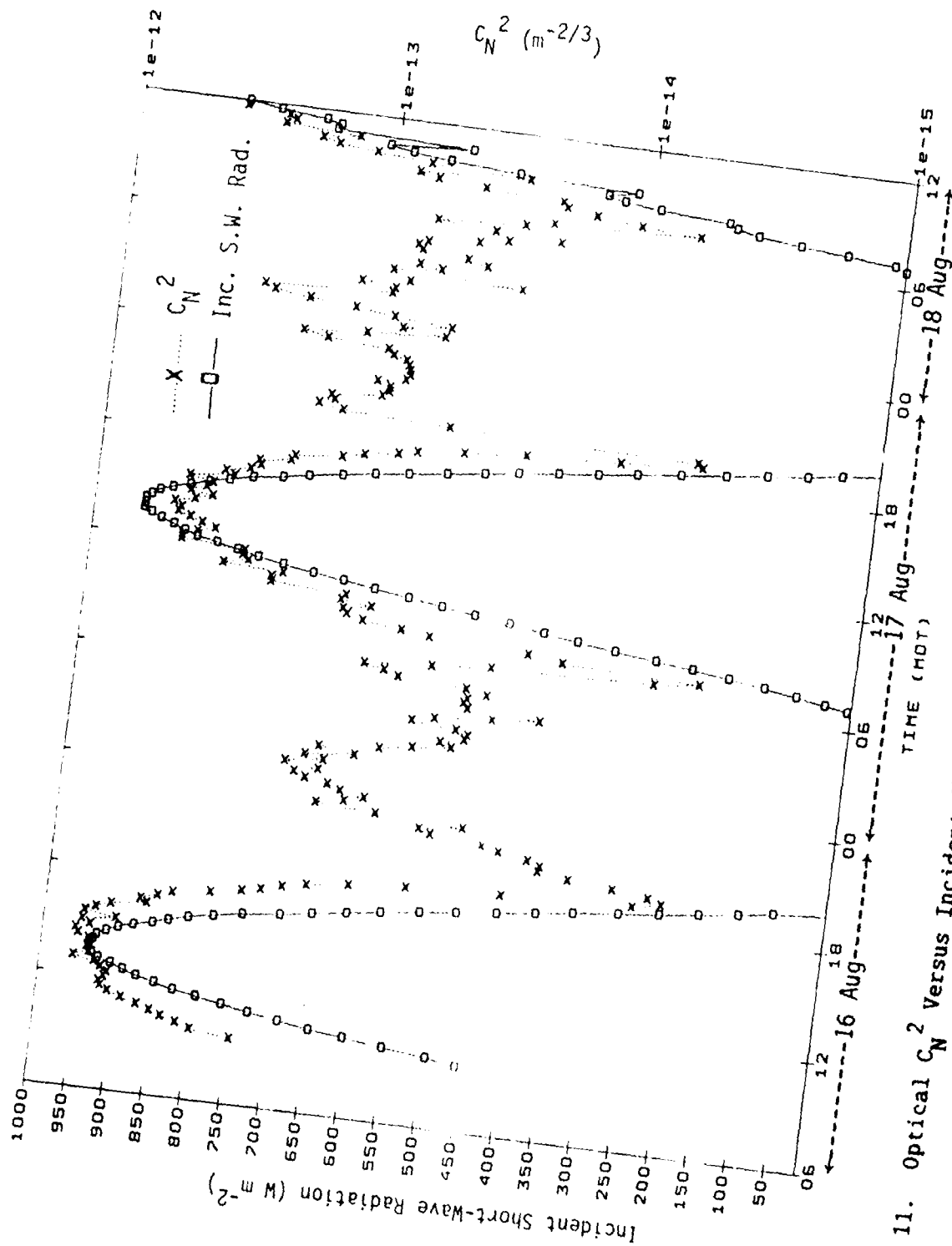


Figure 11. Optical C_N^2 Versus Incident Short-Wave Radiation on 16 - 18 August 1988.

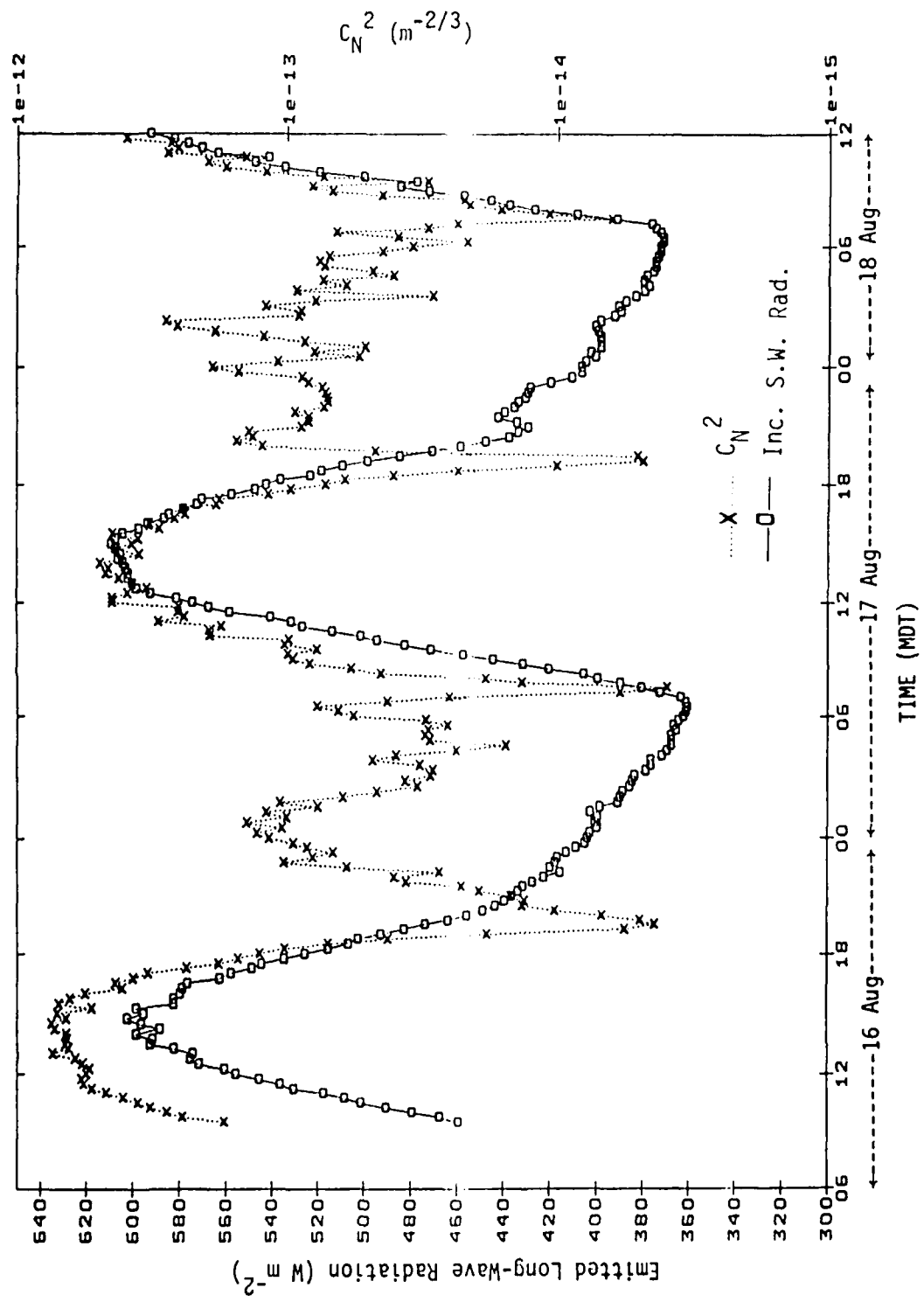
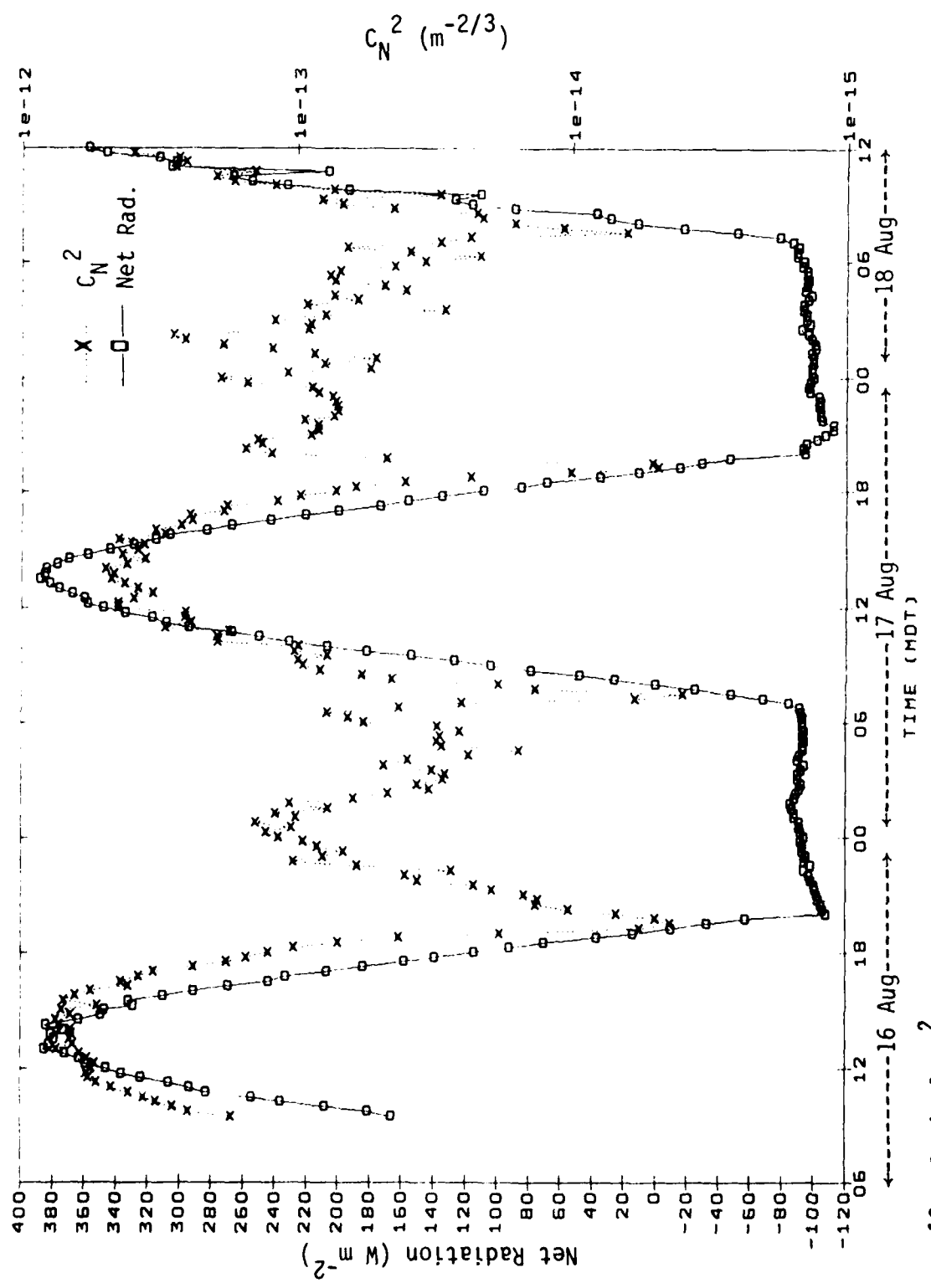


Figure 12. Optical C_N^2 Versus Emitted Long-Wave Radiation on 16 - 18 August 1988.



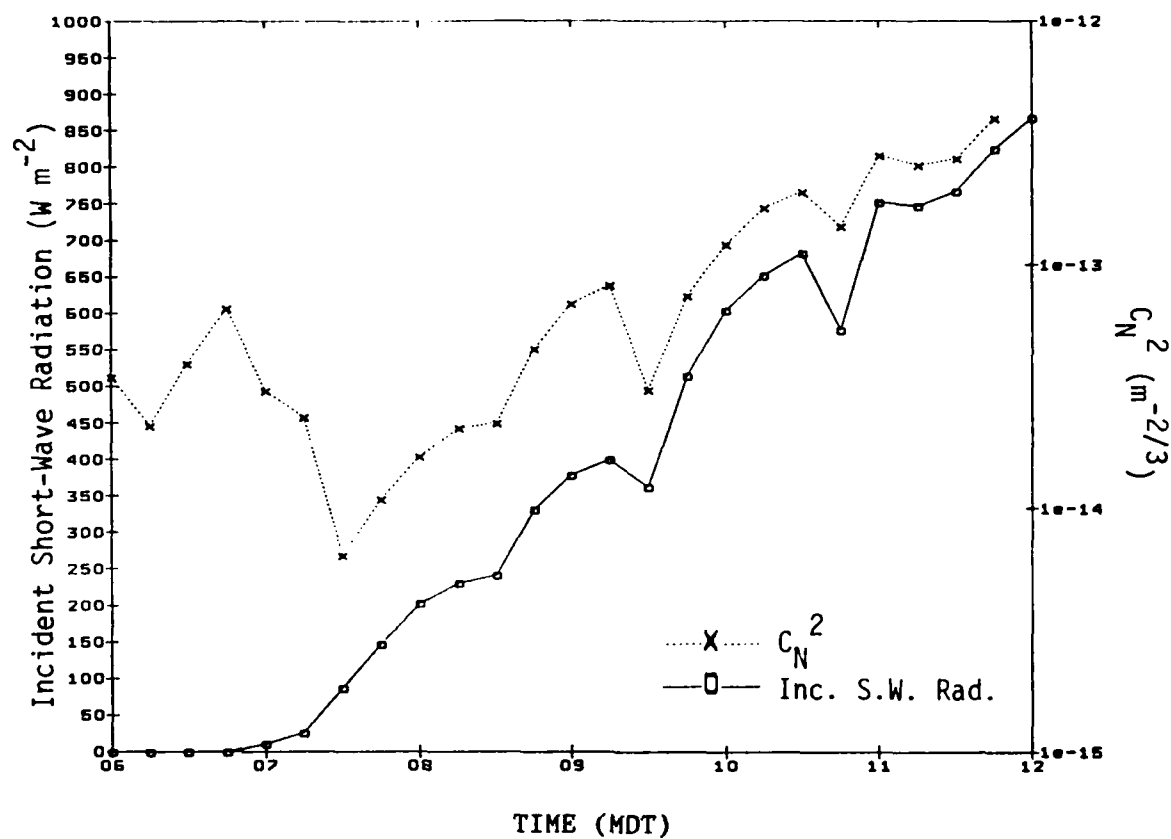


Figure 14. Optical C_N^2 Versus Incident Short-Wave Radiation on 18 August 1988.

INTENTIONALLY BLANK

SECTION 3. APPENDICES

APPENDIX A: A DESCRIPTION OF SCINTILLOMETER OPERATION

Scintillometer operation is based on certain assumptions about atmospheric turbulence. Consequently, scintillometer performance is dependent on how well the atmosphere conforms to these assumptions. The atmosphere is continuously adjusting to the flux of heat by turbulent mixing, which creates a spectrum of turbulent elements (eddies) of varying densities. Density discontinuities between eddies cause changes in the atmospheric refractive index. A model of turbulence initially proposed by Kolmogorov is applied to the refractive index power spectrum. The model depicts a refractive-index spectral density proportional to C_N^2 , representing the strength of refractive index fluctuations. Tatarskii (1961) defines C_N^2 as a function of differences in the refractivity (N) at position x and at scalar separation distances (x+r) within the inertial subrange.

$$\overline{C_N^2} = \overline{(N(x) - N(x+r))^2} / r^{2/3} \quad (A-1)$$

where the overbar indicates a time-averaged quantity.

The Kolmogorov model is assumed to represent turbulence in the inertial subrange, a range of eddy sizes from a few millimeters to several meters, increasing as a function of height above the surface. In this model, turbulent energy is injected at the larger eddy sizes (the outer scale) and is transferred to smaller scales as the larger eddies break up. Energy is transferred to progressively smaller scales essentially without loss until the dissipation range (inner scale) is reached. In the dissipation range, turbulent energy is converted to heat through viscous dissipation. The real atmosphere differs in varying degrees from the ideal turbulent state presented in this model, which assumes the existence of steady-state uniform turbulence. Also, density discontinuities may be very weak in near-neutral conditions. These factors constrain the precision and range of measurements made by wave propagation techniques.

Scintillometers are designed to operate using turbulence scales within the inertial subrange. The principle of optical scintillometer operation can be illustrated with a simple eddy model presented by Clifford et al. (1974). Figure A-1 shows an optical path (0Λ), established between the transmitter and receiver, and a turbulent eddy of radius r at path position ζ . The turbulent eddy represents a density discontinuity moving across the optical path, and its index of refraction creates a new path 0Λ . This eddy is illuminated by a spherical wave of wavelength λ . The illuminated eddy produces a diffraction pattern observed at Λ , the size and contrast of which are determined by ζ , r , λ , and the refractivity fluctuation ΔN of the eddy. Eddies at path position ζ which satisfy the condition $0\Lambda - 0\zeta = \lambda/2$ produce strong scintillations at Λ through destructive interference. This condition is satisfied by a Fresnel-zone size eddy of radius

$$r = [\lambda\zeta(1-\zeta/\Lambda)]^{1/2} \quad (A-2)$$

Eddies of radius larger or smaller than r have focal lengths shorter or longer than Λ and therefore contribute less to the variance in irradiance received at Λ . Sensitivities to the various portions of the optical path are defined by weighting functions. Weighting functions are determined by appropriate transmitter-receiver aperture designs.

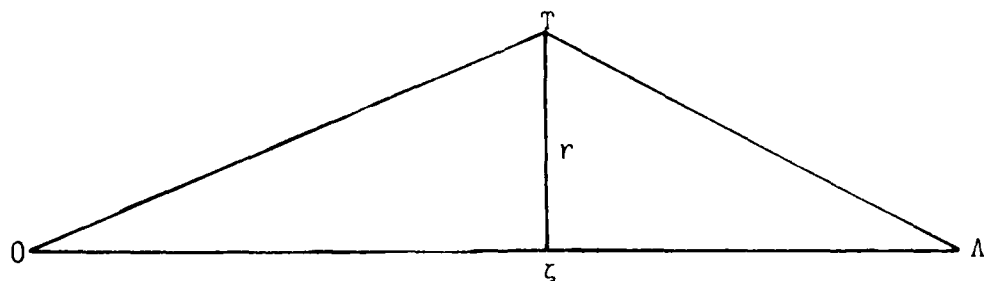


Figure A-1. The Geometry of a Simple Eddy Model Consisting of a Source 0 Illuminating an Eddy of Radius r at Position ζ Along the Optical Path. The Resultant Scintillations are Observed at Position Λ (After Clifford et al., 1974).

The variance in received irradiance is related to C_N^2 through the Tatarskii (1961) first order theory of scintillation. This theory is based on simple superposition of the effects of independent eddy encounters along the path. It predicts that, for a given path length Λ and free-space wavenumber K ($K=2\pi/\lambda$), the proportionality relationship between the log-amplitude variance in irradiance of the spherical wave (σ_t^2) and C_N^2 is

$$\sigma_t^2 = 0.124 K^{7/6} \Lambda^{11/6} C_N^2 \quad (A-3)$$

Equation (A-3) is valid for σ_t^2 less than 0.3. In stronger turbulence, the illuminating wavefront is no longer spherical due to distortion by previous eddies, and the proportionality between C_N^2 and σ_t^2 no longer remains constant. This condition, known as saturation, constrains the length of the optical path over which the scintillometer can be operated. Saturation and the signal-to-noise ratio, which decreases with path length, are the two major constraints on instrument range.

INTENTIONALLY BLANK

APPENDIX B: DESCRIPTION OF DPG SPECTRUM ANALYSIS PROGRAM

Spectrum analysis of time series data provides statistical measures of instrument performance and insight into the physics governing the interactions between sets of time series data. Simple linear correlation coefficients are not applicable to time series data because significance tests are based on the hypothesis that the variate samples are uncorrelated. Because significant autocorrelation often exists in time series data, this hypothesis is seriously violated. Also, the true relationship between two time series can be obscured by an in-phase relationship at some frequencies and an out-of-phase or phase-lagged relationship at other frequencies. A solution to some time series analysis problems lies in the multivariate analyses applied to spectra of time series. These analyses can be accomplished after a Fourier transformation of the series from the time domain to the frequency domain. Transformation partitions the power (energy expenditure per unit time) of the time series into harmonic frequency components. For a given variable, "power" is equivalent to variance in that variable per unit time. The total power of the process is equal to the sum of the contributions by the harmonic components. The advantage of power spectrum analysis over the usual multivariate analysis is that the amount of power contributed by one harmonic is independent of the amplitudes, phases, and frequencies of the other harmonics in the time series (Koopmans, 1974).

Relationships between two time series can be evaluated by examination of the spectra from the two series and their complex products, the cross spectrum, phase (PHASE), and coherence (COH). The cross spectrum is represented by the cospectrum (COS) and quadrature (QUAD). The cospectrum is analogous to an in-phase covariance between the two spectra, and the quadrature spectrum is a similar measure phase-shifted 1/4 wavelength (90°). COS and QUAD define the cross spectrum covariance components in a Cartesian-like coordinate system, while PHASE and COH express these components in a normalized polar coordinate system. PHASE, a representation of the angular relationship between two spectra, is defined as

$$\text{PHASE} = \text{ATAN2}(\text{QUAD}/\text{COS}), \quad (\text{B-1})$$

where ATAN2 is defined in FORTRAN as the arctangent function expanded to the range $-\pi$ to π . PHASE is presented in degrees. COH, the squared coefficient of coherence, is a measure of the correlation between two time series as a function of frequency given by

$$\text{COH} = (\text{COS}^2 + \text{QUAD}^2) / (\text{SPCTR1})*(\text{SPCTR2}), \quad (\text{B-2})$$

where SPCTR1 and SPCTR2 are the spectral components of time series 1 and 2, respectively. COH is dimensionless and ranges in magnitude from 0 to 1. Statistical significance tests can be applied to coherence data as detailed in Koopmans (1974).

Fourier transformation in the DPG spectrum analysis program is achieved using a modification of the Fast Fourier Transform (FFT) procedures provided to DPG by the NOAA ERL/WPL, as described in Kaimal and Gaynor (1983). The spectra produced by this FFT are logarithmically smoothed and scaled to meter-kilogram-second (MKS) units by multiplying each harmonic component by its frequency. Table B.1 is a sample of spectra and their derived components. Spectral analysis techniques are discussed in detail by Koopmans (1974) and Jenkins and Watts (1968).

Table B.1. Spectra From Trial 1A, Channel 5 (T) and 6(q) Data.

Frequency HZ	SPECTRA DATA SUMMARY					
	SPECTRAL VALUES					
	Spectr ^a (T'T')	Spectr ^a (q'q'')	COS (T'q'')	QUAD (T'q'')	PHASE Deg	COH
0.0020	0.0175667	0.0000034	-0.0001853	-0.0000027	181.	0.582
0.0029	0.0144672	0.0000011	-0.0001148	-0.0000127	186.	0.825
0.0039	0.0869024	0.0000079	-0.0007883	0.0001364	170.	0.927
0.0049	0.0414242	0.0000036	-0.0003323	-0.0000642	191.	0.766
0.0063	0.0456963	0.0000045	-0.0004011	0.0001053	165.	0.832
0.0083	0.1778915	0.0000133	-0.0015203	-0.0000497	182.	0.974
0.0107	0.0733853	0.0000055	-0.0006052	0.0000972	171.	0.926
0.0141	0.1611553	0.0000137	-0.0014603	0.0001042	176.	0.968
0.0189	0.0975598	0.0000063	-0.0007142	0.0000711	174.	0.844
0.0248	0.0953864	0.0000075	-0.0007909	0.0000843	174.	0.887
0.0320	0.1434356	0.0000110	-0.0011914	0.0000648	177.	0.903
0.0417	0.0889597	0.0000073	-0.0007702	-0.0000329	182.	0.916
0.0543	0.1153469	0.0000086	-0.0009583	0.0000238	179.	0.923
0.0708	0.1138459	0.0000079	-0.0009086	0.0000170	179.	0.914
0.0920	0.1053497	0.0000070	-0.0008173	-0.0000068	180.	0.908
0.1197	0.0912712	0.0000064	-0.0007125	0.0000264	178.	0.873
0.1550	0.0768547	0.0000060	-0.0006317	0.0000307	177.	0.867
0.2010	0.0639370	0.0000048	-0.0005009	0.0000179	178.	0.822
0.2606	0.0552272	0.0000044	-0.0004310	0.0000193	177.	0.769
0.3380	0.0502979	0.0000038	-0.0003805	0.0000116	178.	0.764
0.4387	0.0428086	0.0000035	-0.0003198	0.0000213	176.	0.687

APPENDIX C: LIST OF SYMBOLS

A = refractive index coefficient for optical wavelength ($78.7 \times 10^{-6} \text{ K mb}^{-1}$)

A_q = dimensionless mmw sensitivity coefficient for humidity, $\left(\frac{1710q}{T}\right) \times 10^{-6}$

A_T = dimensionless mmw sensitivity coefficient for temperature,
 $-\left(\frac{77.6P}{T} + \frac{1710q}{T}\right) \times 10^{-6}$

B = Bowen ratio (dimensionless) $c_p P w'T' / (\epsilon L_w w'e')$

c = calories

C_q^2 = humidity structure parameter $((g \text{ m}^{-3})^2 \text{ m}^{-2/3})$

C_{Tq}^2 = temperature-humidity cross-structure parameter $((K \cdot g \text{ m}^{-3}) \text{ m}^{-2/3})$

C_N^2 = refractive index structure parameter $(\text{m}^{-2/3})$

C_p = specific heat at constant pressure (0.24 c/g/K)

C_T^2 = temperature structure parameter $(K^2 \text{ m}^{-2/3})$

$^{\circ}\text{C}$ = degrees Celsius

e = water vapor pressure (mb)

e_s = saturation vapor pressure (mb)

g = acceleration due to gravity (9.8 m s^{-2})

H = surface layer sensible heat flux (K m s^{-1})

He = latent heat flux (mb m s^{-1})

H_s = H derived from scintillation techniques (K m s^{-1})

k = Von Karman constant (0.4, dimensionless)

K = absolute temperature, Kelvin

L = Obukhov length, meters ($-u_*^3 \bar{T} / (\text{kg} \sqrt{w'T'})$)

L_w = latent heat of vaporization (586 c g^{-1} at 20°C)

m = meter, or prefix milli-

n = real part of the refractive index

N = refractivity (dimensionless, $N=(n-1)\times 10^6$)

P = pressure (mb)
 q = absolute humidity (g m^{-3})
 q_* = humidity scaling factor ($w'q'/u_*$, g m^{-3})
 R = net radiation (W m^{-2})
 r = scalar separation distance (m)
 r_{Tq} = temperature-humidity cross-structure correlation coefficient ($C_{Tq}^2/C_T C_q$)
 s = second
 T = temperature (K)
 T_* = temperature scaling factor ($w'T'/u_*$, K)
 t = time (s)
 u = horizontal wind speed (m s^{-1})
 V = volt
 w = vertical wind speed (m s^{-1})
 W = watts
 u_* = friction velocity (m s^{-1})
 z = height above the surface (m)
 z_0 = roughness length (m)
 α = dimensionless wavelength-dependent structure parameter coefficient
 ϵ = ratio of molecular weights of water vapor and dry air (0.622)
 γ = water vapor correction factor (dimensionless)
 θ = potential temperature (K)
 κ = free space wavenumber ($1/\text{m}$)
 λ = wavelength (m)
 Λ = optical path length (m)
 ρ = air density (g m^{-3})
 σ_t^2 = log amplitude variance in irradiance
 σ_w = square root of the variance in vertical wind (m s^{-1})

APPENDIX D: REFERENCES

- Biltoft, C. A., 1978: Wind and wind-power potential at Dugway National Test Facility Phase I: wind velocity profiles. DPG Doc. No. DPG-TN-C625A, U.S. Army Dugway Proving Ground, Dugway, UT.
- Clifford, S. F., G. Ochs, and R. Lawrence, 1974: Saturation of optical scintillation by strong turbulence. J. Opt. Soc. Amer., 64, 148-154.
- Coulter, R. L., and M. L. Wesley, 1980: Estimates of surface heat flux from sodar and laser scintillation measurements in the unstable boundary layer. J. Appl. Meteor., 19, 1209-1222.
- Eppley Laboratory Manual, Instrumentation for the measurement of the components of solar and terrestrial radiation, Newport, RI.
- Gossard, E. E., and N. Sengupta, 1988: Measuring gradients of meteorological properties in elevated layers with a surface-based Doppler radar. Radio Sci., 23, 625-639.
- Hill, R. J., S. F. Clifford, and R. S. Lawrence, 1980: Refractive-index and absorption fluctuations in the infrared caused by temperature, humidity, and pressure fluctuations. J. Opt. Soc. Am., 70, 1192-1205.
- Hill, R. J., and S. F. Clifford, 1981. Contribution of water vapor monomer resonances to fluctuations of refraction and absorption for submillimeter through centimeter wavelengths. Radio Sci., 16, 77-82.
- Hill, R. J., R. A. Bohlander, S. F. Clifford, R. W. McMillan, J. T. Priestley, and W. P. Schoenfeld, 1988: Turbulence-induced millimeter-wave scintillation compared with micrometeorological measurements. IEEE Transactions on Geoscience and Remote Sensing, 26, 330-342.
- Izumi, Y., (Ed.) 1971: Kansas 1968 field Program Data Report. Environ. Res. Pap. No. 379, AFCRL-72-0041, Air Force Cambridge Research Laboratories, Bedford, MA, 73 pp.
- Jenkins, G. M., and D. G. Watts, 1968: Spectral Analysis and its Applications. Holden-Days, San Francisco, 525 pp.
- Kaimal, J. C., 1988: The Atmospheric Boundary Layer - Its Structure and Measurement. Indian Institute of Tropical Meteorology, Shivajinaga, Pune, India.
- Kaimal, J. C., and J. E. Gaynor, 1983: The Boulder Atmospheric Observatory. J. Appl. Meteor., 22, 863-880.
- Kohsiek, W., 1982: Measuring C_T^2 , C_q^2 , and C_T^q in the unstable surface layer, and relations to the vertical fluxes of heat and moisture. Boundary-Layer Meteor., 24, 89-107.

- Kondo, J. O. Kanechika, and N. Yazada, 1978: Heat and momentum transfers under strong stability in the atmospheric surface layer. J. Atmos. Sci., 35, 1012-1021.
- Kondratyev, K.YA., 1969: Radiation in the Atmosphere. Academic Press, New York, San Francisco and London, pp 570-80.
- Koopmans, L., 1974: The Spectral Analysis of Time Series. The Academic Press, New York, 366 pp.
- McMillan, R. W., R. A. Bohlander, G. R. Ochs, R. J. Hill, and S. F. Clifford, 1983: Millimeter wave atmospheric turbulence measurements: preliminary results and instrumentation for future measurements. Opt. Eng., 22, 32-39.
- Morgan, D. L., Pruitt, W. O., and Lourence, F. J., 1970: Radiation data analyses for the 1966 and 1967 micrometeorological field runs at Davis, California. Research and Development Tech. Report. ECOM 68-G10-2. U.S. Army Electronics Command, ASL Fort Huachuca, AZ.
- Ochs, G. R., and W. D. Cartwright, 1980: Optical system model IV for space-averaged wind and C_N^2 measurements. NOAA Technical memorandum ERL WPL-52, National Oceanic and Atmospheric Administration, 31 pp.
- Priestley, J. T., and R. J. Hill, 1985: Measuring high-frequency humidity, temperature, and radio refractive index in the surface layer. J. Atmos. and Oceanic Tech., 2, 233-251.
- Sellers, W. D., 1965: Physical Climatology. The University of Chicago Press, Chicago and London, pp. 40-64.
- Tanner, B. D., M. S. Tanner, W. A. Dugas, E. C. Campbell, and B. L. Blank, 1985: Evaluation of an operational eddy correlation system for evapotranspiration measurements. In Proceedings of the National Conference on Advances in Evapotranspiration, Amer. Soc. of Agricultural Engineers, Chicago, IL, pp 87-99.
- Tatarskii, V. I., 1961: Wave Propagation in a Turbulent Medium. Dover, 285 pp.
- Walters, D. L., and Kunkel, K. E., 1981: Atmospheric modulation transfer function for desert and mountain locations: the atmospheric effects on r_0 . J. Opt. Society of Amer., 71, 397-405.
- Wesely, M. L., 1976: The combined effect of temperature and humidity fluctuations on refractive index. J. Appl. Meteor., 15, 43-49.
- Wesely, M. L., and B. B. Hicks, 1978: High-frequency temperature and humidity correlation above a warm wet surface. J. Appl. Meteor., 17, 123-128.
- Wyngaard, J. C., Y. Izumi, and S. A. Collins, Jr, 1971: Behavior of the refractive-index structure parameter near the ground. J. Opt. Society of Amer., 61, 1646-1650.